nature communications

Article

https://doi.org/10.1038/s41467-026-77894-2

PIP5K-Ras bistability triggers plasma membrane symmetry breaking to define cellular polarity and regulate migration

Received: 3 March 2026

Accepted: 4 September 2026

Published online: 30 September 2026

Check for updates

Yu Deng[1,2,13], Tatsat Banerjee[1,2,11,13], Satomi Matsuoka[3], Debojyoti Biswas[4], Liz A. Kurtz[5], Jane Borleis[1], Yu Long[1], Parijat Banerjee[6], Huiwang Zhan[1], Dhiman Sankar Pal[1,7,12], Nathan H. Roy[5], Masahiro Ueda[3], Pablo A. Iglesias[1,8,9] & Peter N. Devreotes[1,10]

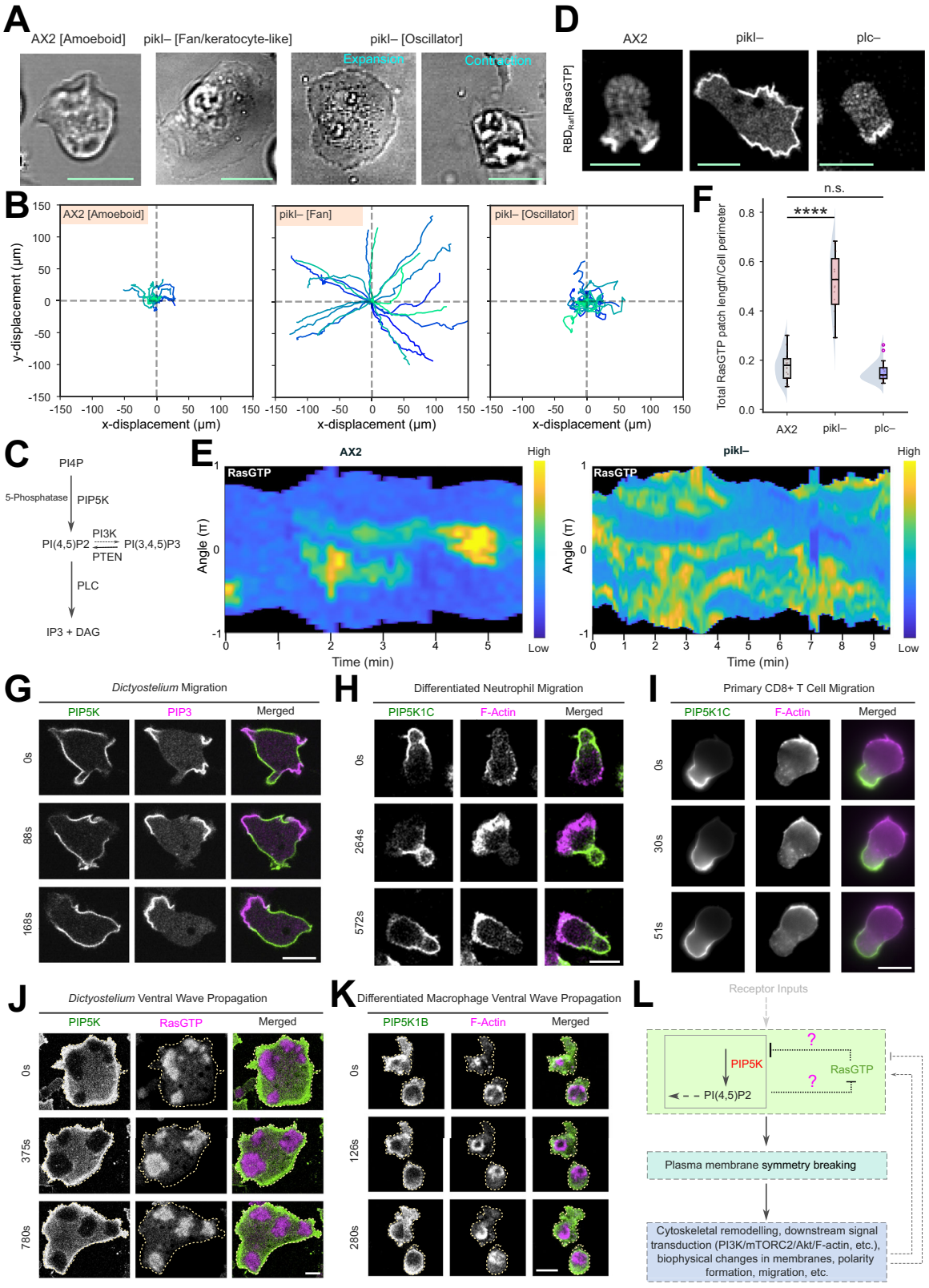
An initial break in plasma membrane symmetry triggers hundreds of spatiotemporally controlled signaling and cytoskeletal events that regulate cell polarization during migration and macropinocytosis. However, the mechanism driving this self-organizing transition remains unknown. Using *Dictyostelium* amoebae, leukocytes, cancer cells, and 3D organoids, we show that mutual antagonism between activated Ras and phosphatidylinositol 4-phosphate 5-kinase (PIP5K) forms a positive feedback loop fundamental to symmetry breaking and cell polarity. Through dynamic localization mapping, optogenetic perturbation, RasGEF screening, and single-molecule tracking, we reveal that localized Ras activation shortens the membrane lifetime of PIP5K, lowering local PI(4,5)P2, while recruited RasGEF amplifies Ras activation. Dissociated PIP5K redistributes to other membrane domains, suppressing local Ras activation and intrinsically segregating the membrane into complementary activated and inactivated zones, independent of receptor inputs or cytoskeletal dynamics. Incorporating this feedback loop into an excitable network integrated with a reaction-diffusion model and a viscoelastic framework yielded computational simulations that accurately predict spatiotemporal self-organization and polarized cell movement.

Cells display an extraordinary ability to spontaneously break symmetry and adopt a wide range of morphological forms. These dynamics are essential for cellular and developmental processes underlying normal physiology, and their disruption is linked to disease states in which cells fail to grow, move, or differentiate properly, including congenital defects, impaired tissue regeneration, immune dysfunction[1], and cancer invasion[2,3]. The morphological changes depend on the segregation of the plasma membrane and associated cortex into two complementary states. For example, during directed migration, a cell maintains distinct "front" and "back" regions of the membrane/cortex, where specific sets of signaling and cytoskeletal components self-organize[4–8]. Notably, the complementarity between the molecular components that define the "front" and "back" regions during migration is conserved across various physiological processes, such as ventral wave propagation[9], macropinocytosis[10,11], phagocytosis[12], cytokinesis, and apical-basal polarity formation in epithelial cells[13].

The importance of front-back asymmetry in cell migration has long been recognized, but conceptual paradigms often conflate distinct phenomena such as symmetry breaking, polarity, motility, and directional sensing. *Symmetry breaking* refers to the initial redistribution and segregation of otherwise homogeneous surface molecules, which can occur even in immobilized, round cells devoid of cytoskeletal dynamics[14–28]. In the presence of an external gradient, these

A full list of affiliations appears at the end of the paper. e-mail: pnd@jhmi.edu

https://doi.org/10.1038/s41467-026-77894-2



localizations reflect *directional sensing*, which can occur before any changes in cell shape or movement. *Motility* emerges when this asymmetry is coupled to cytoskeletal activity, leading membrane-cortex domains with front or back components to protrude and contract, respectively. *Polarity* establishes a stable morphological front/back axis, restricting protrusions and associated molecules primarily to the front of a migrating cell. *Directed migration* integrates these processes to enable detection of and movement toward external cues[5,29,30]. Numerous hypotheses for directional sensing and polarity have been proposed, either involving a local activator and a more global inhibitor to allow localized responses while suppressing protrusive activity elsewhere or involving a local pseudopod-inhibition

Fig. 1 | Deleting PIP5K increases cell migration speed, hyperactivation of Ras/PI3K/F-actin network; the enzyme dynamically localizes into the back-state regions of the plasma membrane. A Representative live-cell DIC images of wild-type AX2 and *pikI*− *Dictyostelium* cells. For all main and Supplementary Figs., all scale bars represent 10 μm, unless otherwise mentioned. **B** Centroid tracks of randomly migrating AX2 and *pikI*−*Dictyostelium* cells. Here $n_c = 20$ cells are shown for each migration mode and each cell was tracked for 8 min and was reset to the same origin. **C** Schematic showing major pathways for synthesizing and degrading PI(4,5)P2 on the plasma membrane. **D** Representative live-cell images of wild-type AX2 cells (left), *pikI*−cells (middle), and *plc*-cells (right) expressing RBD-GFP. Ras-Binding Domain (RBD) of Raf1 was used as a biosensor of Ras activation. **E** Representative 360° membrane kymograph (see "Methods" for details) of RBD-GFP intensity in AX2 (left) and *pikI*− cells (right), respectively, corresponding to Fig. 1D. **F** Quantification of overall RasGTP level on the cell membrane in AX2, *pikI*−, and *plc*− cells, expressed as total RBD patch length/cell perimeter. Here, $n_c = 20$ (AX2), 21(*pikI*−), or 24 (*plc*−) cells; here (and elsewhere), each of the nc cells were tracked for at least nf = 5 frames and the average values were obtained. Throughout this study, boxes, whiskers, and outliers are graphed as per Tukey's convention and the kernel density plots are shown on the left. The *p* values are computed by the Mann-Whitney U test. **G** Representative live-cell images of *Dictyostelium* cells coexpressing PIP5K-GFP and PHcrac-mCherry during migration. **H,I** Live-cell images of migrating differentiated HL-60 neutrophils (**H**) or mouse primary CD8 + T cells (**I**) coexpressing PIP5K1C-GFP and LifeAct-iRFP703 or PIP5K1C-mNeon and LifeAct-mScarlet3, respectively. **J** Live-cell images of *Dictyostelium* cells coexpressing mRFP-PIP5K and RBD-GFP during ventral wave propagation. **K** Live-cell images of HL-60 cells (differentiated into macrophages) coexpressing PIP5K1B-GFP and LifeAct-iRFP703. **L** Schematic showing a potential core signaling network involving mutually antagonistic interaction between PIP5K and activated Ras.

system[31–45]. However, most polarity models require mechanical activity by the functional cytoskeleton and thus cannot explain the initial molecular segregation step, whereas directional sensing models depend on external cues and therefore cannot account for spontaneous, cell-intrinsic symmetry breaking.

A key initial symmetry-breaking event on the membrane is the spontaneous local activation of the oncogene Ras, which correlates with a local decrease in negative surface charge on the inner leaflet of the lipid bilayer[13,25,46]. Activated Ras is found in the front of the migrating cells[21,27,47–50], macropinosomes[51–53], and in the "front" state regions of the propagating cortical waves, which are also enriched in PIP3, Akt, and F-actin[9,13,17,25,26,54–57]. Patches of activated/GTP-bound Ras can appear on the membrane of a cell, even in cells lacking functional cytoskeletons or with impaired receptor modules[16,22,36,58–60]. An important determinant of surface charge is PI(4,5)P2 (PIP2), which is depleted in membrane regions where Ras activity is high[25,59,61–64]. Moreover, artificially lowering PI(4,5)P2 increases the size of protrusions and the frequency of spontaneous Ras patches in *Dictyostelium* and human epithelial cells[16,17,47]. It is well-documented that PI(4,5)P2 plays a central role in numerous cellular physiological processes[65–68]. Many PI(4,5)P2-binding proteins have been reported, and many other roles have been attributed to PI(4,5)P2. This raises the question of whether PI(4,5)P2 positively or negatively regulates migration, signal transduction, and cytoskeletal activities in vivo, and how PI(4,5)P2 is locally regulated.

In this study, we identify a core positive feedback loop in which mutual inhibition between PIP5K and RasGTP drives symmetry breaking and regulates cell polarity and migration. Across diverse cell types, PIP5Ks dynamically localize to posterior membrane regions, complementary to domains where the Ras/PI3K/F-actin network is active; accordingly, deleting PIP5K causes signaling hyperactivation and a dramatic increase in migration speed, whereas conditional PIP5K overexpression virtually eliminates Ras/PI3K/F-actin signaling, impairs ventral wave propagation, desensitizes cells to receptor stimulation, and blocks migration in both two and three dimensions. Remarkably, this circuit regulates symmetry breaking and signaling outputs even in cells lacking cytoskeletal dynamics or receptor modules. Mechanistically, local reduction of PIP5K/PI(4,5)P2 facilitates recruitment of a specific RasGEF, amplifying Ras activation through positive feedback, while single-molecule measurements show that GTP-bound Ras reduces the membrane lifetime of PIP5K molecules, which then relocate to other membrane domains where they suppress Ras activation. We further developed a computational framework that embeds this self-amplifying circuit within an excitable network topology and couples it to a viscoelastic model of morphological change, predicting how tuning PIP5K activity modulates signaling, wave propagation, and cell migration mode.

Results

Loss of PIP5K alters migration and activates the Ras/PI3K network

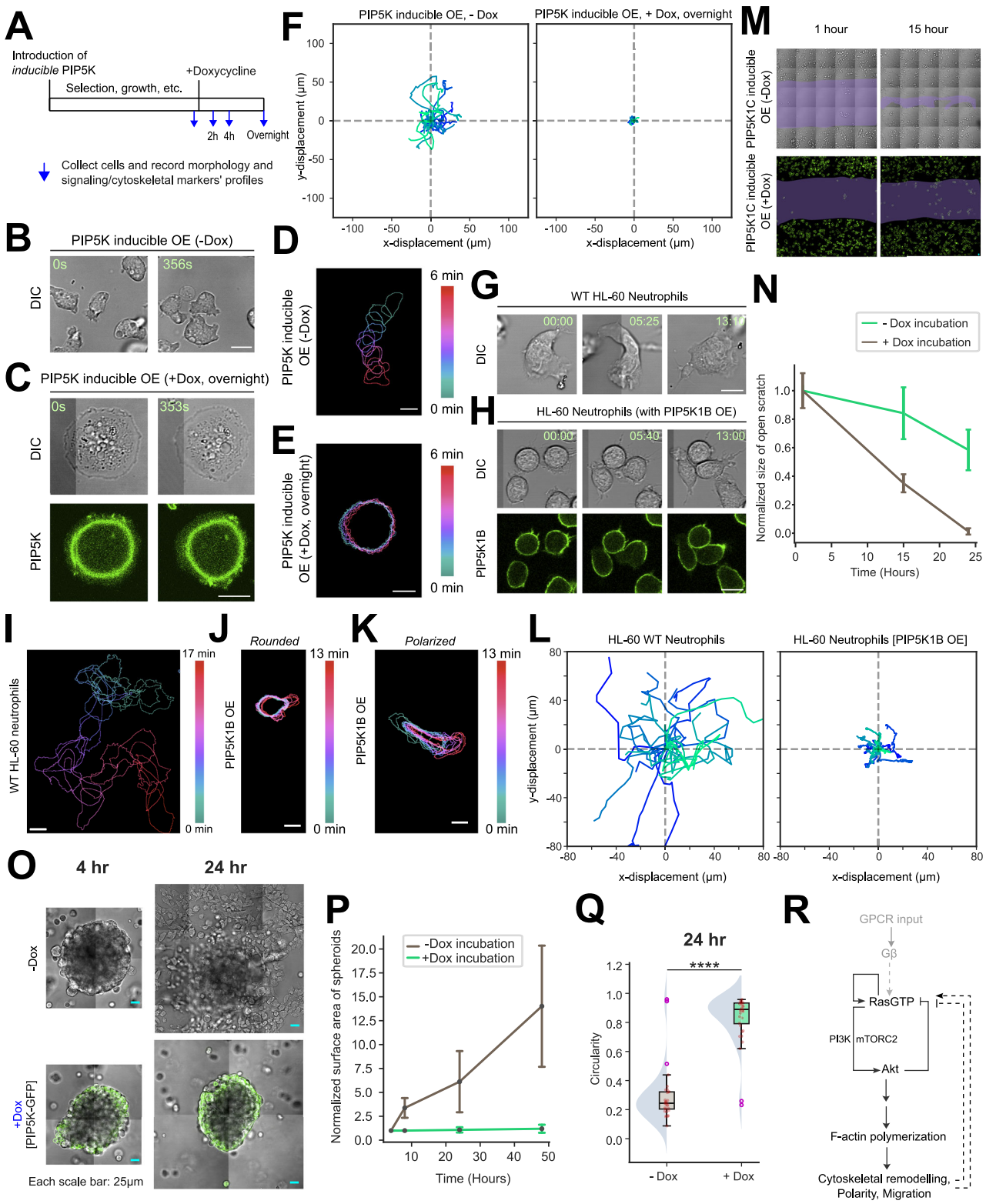
A report of normal migration in *pikI*$^-$ cells[69], which lack the sole PIP5K gene in *Dictyostelium*, conflicted with the dramatic phenotype switch from amoeboid to oscillatory and fan-shaped cells caused by synthetic PI(4,5)P_2 depletion[16], prompting us to reexamine this issue. Compared to WT cells, *pikI*- cells displayed a vast increase in fan-shaped and oscillatory cells, resembling the PI(4,5)P2 depletion phenotype (Fig. 1A and Supplementary Movie 1). To quantify these migratory modes, we developed an automated hierarchical cell-classification algorithm (Supplementary Figs. 1A, B and 2A–G, see "Methods"). The properties of *pikI*- cells were documented: the fan-shaped and oscillatory cells migrated more rapidly and had a larger basal area (Fig. 1B and Supplementary Fig. 3A–D). Interestingly, when grown in shaking culture, most *pikI*- cells become multinucleated (Supplementary Fig. 3E, F), presumably due to cytokinesis defects. However, when cultured adherently, over 70% of fan-shaped cells remained mononucleated (Supplementary Fig. 3G, H). These migration defects likely explain the inability of *pikI*- cells to chemotax, aggregate, and form multicellular structures in a timely fashion (Supplementary Fig. 3I).

In addition to PIP5K, PI(4,5)P2 levels can, in theory, be altered by PI3K, PLC, PTEN, and PI 5-phosphatases (Fig. 1C). While deleting PI3Ks, PLC, or PI 5-phosphatases alters migration, the effects are minor compared to those caused by the loss of PIP5K (Supplementary Fig. 4A–E)[69–73]. Cells lacking PTEN become adherent and "freeze" in place, unlike the extremely active *pikI*- cells.

To further understand the basis of *pikI*- cell phenotypes, we examined a series of signal transduction and cytoskeletal activities using specific biosensors. As expected, $PH_{PLC\delta}$ localized mainly to the membrane of WT cells, indicating high PI(4,5)P2 levels, but showed no apparent membrane association in *pikI*- cells (Supplementary Fig. 4F, G and Supplementary Movie 2). Next, we examined the spatial distribution of "front"-state markers in WT, *pikI*-, and *plc*- cells. Compared with WT and *plc*- cells, which have characteristic patches of the RasGTP-binding domain, RBD, at the cell protrusions (Supplementary Movie 3), *pikI*- cells have much wider patches, corresponding to the broader protrusions (Fig. 1D–F, Supplementary Fig. 4C and Supplementary Movie 3). LimE, an F-actin biosensor, also displayed much larger patches in *pikI*- cells, compared with WT and *plc*- cells (Supplementary Fig. 4D, E, H–J and Supplementary Movie 4). Similar results were observed with a PIP3 biosensor (Supplementary Fig. 4K, L and Supplementary Movie 4). When oscillating cells spread, activities increase dramatically and disappear upon cell shrinking (Supplementary Fig. 4M). It is well known that PI3K only converts a small portion of PI(4,5)P2 to PIP3, so it is not surprising that the remaining PI(4,5)P2 in *pikI*- cells is sufficient to serve as the substrate[69,74].

Next, we examined signal transduction and cytoskeletal activities typically associated with the "back"-state of cells, such as PI(3,4)P2 and cortical myosin. Strikingly, there generally was no detectable PI(3,4)P2

https://doi.org/10.1038/s41467-026-77894-2



in *pikI*- cells, as shown by PHcynA, a biosensor that reports the level of PI(3,4)P2 (Supplementary Fig. 4N and Supplementary Movie 5)[75,76]. Cortical myosin was also greatly reduced (Supplementary Fig. 4O and Supplementary Movie 5). Since Ras activity is elevated in *pikI*- cells, and it is known that there are mutually inhibitory interactions between Ras and PI(3,4)P2 and Ras and myosin II, these reductions are likely indirect. Taken together, our data show that loss of PIP5K activates the Ras/PI3K/Akt/F-actin network and simultaneously decreases "back" state signaling, suggesting that PIP5K is a general negative regulator.

PIP5Ks localize to back-state regions of the membrane

Since PIP5K deletion activates cells, we wondered how PIP5K localizes relative to activated regions in WT cells, and we examined protrusion formation and ventral wave propagation across a wide array of cell systems. First, we co-expressed PIP5K with a typical front-state marker,

Fig. 2 | Inducible overexpression of PIP5Ks impairs cell migration and polarity in an evolutionarily conserved fashion. A Schematic of the experimental strategy involving doxycycline-inducible promoter-driven PIP5K overexpression. **B, C** Live-cell images of *Dictyostelium* cells expressing doxycycline (Dox)-inducible PIP5K-GFP without (**B**) or with overnight Dox induction (**C**) **D, E** Color-coded temporal overlay profiles of *Dictyostelium* cells expressing Dox inducible PIP5K-GFP without (**D**) or with overnight Dox induction (**E**) **F** Centroid tracks of randomly migrating *Dictyostelium* cells ($n_c = 20$) expressing Dox inducible PIP5K, without (left) or with overnight (right) Dox treatment. Each cell was tracked for 10 min and was reset to the same origin. **G, H** Migrating differentiated HL-60 neutrophils. Time in min:s format. **I–K** Color-coded temporal overlay profiles of differentiated WT HL-60 (**I**), or neutrophils overexpressing PIP5K1B-GFP (rounded) (**J**), or neutrophils over-expressing PIP5K1B-GFP (polarized) (**K**). **L** Centroid tracks of migrating differentiated WT HL-60 cells (left), or neutrophils overexpressing PIP5K1B-GFP (right). Each of these $n_c = 20$ tracks is 12 min and was reset to the same origin. **M** Representative live-cell images of MDA-MB-231 cells in wound healing assay, expressing Dox-inducible PIP5K1C-GFP, either without or with overnight Dox treatment. DIC images are shown for cells that were incubated without Dox and GFP channel are shown for cells that were incubated overnight with Dox. Images were acquired at respective time points. Purple color overlay was used to show the wound area. **N** Normalized size of the open scratch at different timepoints. Open scratch area at each time was normalized to scratch area at 1 h. Here, data from $N \geq 3$ independent experiment and n: For PIP5K1C: 7 (1 h), 8 (15 h), 7 (24 h). For WT: 5 (1 h), 8 (15 h), 7 (24 h). Error bars: SD. **O** Representative live images at 4hr and 24hr from embedding of organoids incubated without Dox (DIC alone) or after overnight incubation with Dox (merged GFP+DIC). Scale bars represent 10 µm. **P** Normalized surface area of organoids at different time points after embedding in Matrigel. n: for-Dox: 14 (4 h), 10 (8 h), 33 (24 h), 32 (48 h); for +Dox: 15 (4 h), 15 (8 h), 36 (24 h), 38 (48 h) spheroids. Error bars: SD. **Q** Circularity of the organoids incubated with or without Dox at 24 h. $n = 33$ (−Dox, 24 h), 36 (+Dox, 24 h); p value by two-tailed Mann−Whitney U test. **R** Simplified schematic of the signal transduction network that is known to control cytoskeletal structures, cell polarity, and migration. As the network can act independent of receptor inputs, receptor modules are shown in gray. Dashed black lines show putative positive and negative feedback from the downstream cytoskeletal network to the upstream signaling network.

PIP3, in *Dictyostelium* cells. PIP5K was depleted from protrusions and localized complementary to PIP3 (Fig. 1G and Supplementary Movie 6). PIP5K that was depleted from the protrusions did not appear in the cytosol, and the total amount of PIP5K on the membrane remained consistent.

This back localization was conserved for PIP5K1B and PIP5K1C in HL60 neutrophils during random migration (Fig. 1H, Supplementary Fig. 5A and Supplementary Movie 6); previous reports showed these enzymes localize to the uropod during chemotaxis[63,64]. Consistently, PIP5K1C localized towards the back regions in mouse CD8+ primary T cells, opposite to F-actin (Fig. 1I, Supplementary Fig. 5B and Supplementary Movie 7). In addition, in MDA-MB-231 cancer cells, PIP5K1B and PIP3 exhibited complementary localizations (Supplementary Fig. 5C and Supplementary Movie 7).

We then examined the spatiotemporal profile of PIP5K during spontaneous wave propagation in electro-fused *Dictyostelium* cells[9] and frustrated phagocytosis in HL-60 macrophage-like cells[62]. In these seemingly diverse scenarios, PIP5K was depleted in front-state regions marked by high PI3K, Ras, or F-actin activity (Fig. 1J, K, Supplementary Fig. 5D–F, and Supplementary Movie 8). As expected, PIP5K and its product, PI(4,5)P2, were co-localized in the back-state regions (Supplementary Fig. 5G and Supplementary Movie 8). Collectively, these results demonstrate that, during protrusion formation or wave propagation, PIP5Ks consistently localize to back-state regions, in an evolutionarily conserved fashion (Supplementary Fig. 5H).

Although PIP5K is robustly membrane-associated, it lacks a recognizable membrane-association or transmembrane domain. To identify PIP5K structural domains controlling membrane binding and trailing-edge accumulation, we generated truncation constructs and examined their localization in *Dictyostelium* cells (Supplementary Fig. 6A and Supplementary Movie 9). $PIP5K_{301\text{-}718aa}$ localized largely to the plasma membrane, like full-length PIP5K, with some cells showing tighter back-state localization (Supplementary Fig. 6B and Supplementary Movie 9). In contrast, the N-terminal 315 aa was not membrane-localized. $PIP5K_{316\text{-}718aa}$ was largely cytosolic, although its membrane-associated fraction was not back-localized (Supplementary Fig. 6C, D and Supplementary Movie 9). Synthetic membrane recruitment did not restore back localization to either fragment (Supplementary Fig. 6C, D). Thus, residues 301–316 are important for membrane localization at the back, and the membrane- and back-localization signals were not easily separable, suggesting that back localization may require coincident association of two independent sequences within PIP5K.

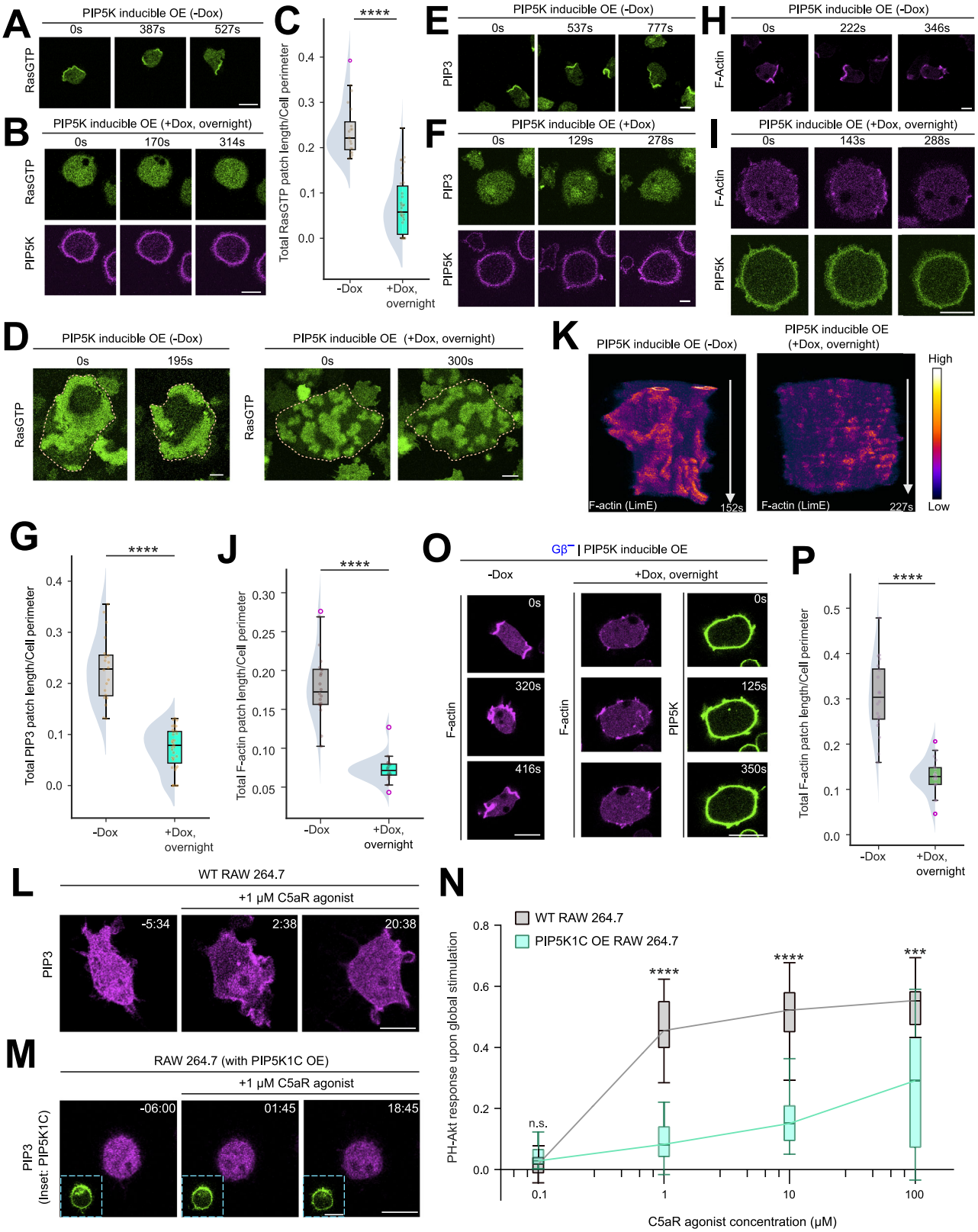
Taken together, our results indicate that (1) PIP5K is the major regulator of local PI(4,5)P2 levels on the membrane; (2) PI(4,5)P2 is a negative regulator of the Ras/PI3K/F-actin network; (3) PIP5K dissociates from protrusions with elevated Ras activity and localizes elsewhere. This suggests that a mutually inhibitory Ras-PIP5K circuit is important for breaking membrane symmetry. We surmise that "downstream" signaling cascades such as PI3K/mTORC2/Akt reinforce this initial asymmetry, and as cytoskeletal activities remodel, polarity forms, and cells effectively migrate (Fig. 1L).

Overexpressing PIP5Ks suppresses cell protrusions and tunes migration

To assess how PIP5K expression affects migration and cellular activities, we developed a conditional doxycycline-inducible PIP5K overexpression system (Fig. 2A). Without doxycycline (Dox) induction, *Dictyostelium* cells show their normal amoeboid behavior (Fig. 2B and Supplementary Movie 10). Upon overnight Dox induction, two striking phenotypes appeared in the overexpressing (OE) cells. Approximately 55% of the cells rounded up, lacking protrusions (Fig. 2C, Supplementary Fig. 7A, and Supplementary Movie 10), while the remaining cells had numerous tiny, broken protrusions, resembling short filopodia, along their perimeter (Supplementary Fig. 7B and Supplementary Movie 10); migration was severely impaired in both cases (Fig. 2D–F and Supplementary Fig. 7C, D). These cells were flatter, occupied more surface area, and were less polarized (Supplementary Fig. 7E–G); these properties depend on the expression levels (Supplementary Fig. 7H). When we applied a chemotactic gradient (Supplementary Fig. 8A), overall chemotaxis was strongly impaired in PIP5K OE cells. A fraction of cells migrated poorly towards the folic acid source (possibly the spiky cells became polarized), and the rest did not migrate at all (Supplementary Fig. 8B–E and Supplementary Movie 11). Surprisingly, cells with very low PIP5K expression after 2 h Dox incubation became elongated and migrated faster (Supplementary Figs. 7D, F–H, 8F–H and Supplementary Movie 12). A similar increased speed was observed in cells expressing a PIP5K mutant (K681N, K682N), which has impaired kinase activity (Supplementary Figs. 7D, 8I, J and Supplementary Movie 12)[77]. While increasing PIP5K activity strongly inhibits migration, the slight improvements from small increases likely reflect bringing the elevated Ras activity in axenic WT cells into range[52]. Further characterization of OE cells showed that macropinocytosis was significantly reduced (Supplementary Fig. 8K–M). Surprisingly, while *pikI-* cells have very elevated PIP3, a marker for macropinocytosis[78–80], FITC-dextran uptake was also severely impaired in these cells (Supplementary Fig. 8M). Together, these results suggest that cell morphology, macropinocytosis, and migration depend critically on context-dependent, optimal PIP5K activity.

Since the localization of PIP5K was conserved from *Dictyostelium* to a series of mammalian leukocytes and cancer cells, we next tested whether the physiological roles of the enzymes were also conserved.

https://doi.org/10.1038/s41467-026-77894-2



First, upon overexpressing either PIP5K1B or PIP5K1C in neutrophils, cells became either more elongated than WT, with PIP5Ks enriched on the tail (Fig. 2G, Supplementary Fig. 9A, B and Supplementary Movie 13) or rounded with PIP5Ks broadly distributed on the membrane (Fig. 2H, Supplementary Fig. 9C, and Supplementary Movie 13). The overall migration speed and cell areas were substantially reduced (Fig. 2I–L and Supplementary Fig. 9D–H). Overlayed cell profiles showed that the leading edge of the polarized cells was active, but the tail appeared to adhere more strongly to the surface (Fig. 2K and Supplementary Fig. 9G). Similar phenotypes were observed when recruiting Rasal3 to the membrane in HL-60 neutrophils[60]. Cells with rounder shapes have higher PIP5K expression levels (Supplementary Fig. 9I, J), consistent with the *Dictyostelium* results. Second, overexpression of PIP5K1B and PIP5K1C in

Fig. 3 | Inducible overexpression of PIP5Ks inhibits spontaneous and receptor driven signal transduction and cytoskeletal activities. A, B Live-cell images of *Dictyostelium* cells co-expressing RBD-GFP and Dox-inducible mRFP-PIP5K without (**A**) or with overnight Dox induction (**B**). **C** Quantification of overall RasGTP level on the cell membrane in *Dictyostelium* cells expressing Dox-inducible mRFP-PIP5K, without or with Dox induction. The levels are expressed as total RBD-GFP patch per unit perimeter length. Here, nc = 31 (+Dox overnight), or 20 (−Dox) cells. The *p* values are computed by the Mann−Whitney U test. **D** Ventral wave propagation in *Dictyostelium* cells co-expressing RBD-GFP and Dox-inducible mRFP-PIP5K, without (left) or with overnight Dox induction (right). **E, F** Live-cell images of *Dictyostelium* cells co-expressing PHcrac-YFP and Dox-inducible mRFP-PIP5K without (**E**) or with overnight Dox induction (**F**). **G** Quantification of overall PIP3 level on the cell membrane in *Dictyostelium* cells with Dox-inducible mRFP-PIP5K overexpression system, without or with Dox induction. The levels are expressed as total PHcrac-YFP patch length per unit perimeter length. Here, nc = 35 (+Dox overnight), or 20 (−Dox) cells. The *p* values are computed by the Mann−Whitney U test. **H, I** Live-cell images of *Dictyostelium* cells co-expressing LimE-mCherry and Dox-inducible GFP-PIP5K without (**H**) or with overnight Dox induction (**I**). **J** Quantification of newly polymerized F-actin level on the plasma membrane in *Dictyostelium* cells, either without or with overnight Dox treatment. The levels are expressed as total actin patch length per unit cell perimeter length. For overnight Dox treatment case, only spiky populations are included and round population (showing no patches) has been excluded. Here, nc = 20 for all populations; data from $N = 3$ independent experiments; *p* value by the two-tailed Mann−Whitney U test. **K** Two t-stacks (see Methods) from cells co-expressing LimE-mCherry and Dox-inducible GFP-PIP5K without (left) or with overnight Dox induction (right). The white arrow corresponds to the time duration of the t-stack. **L, M** Live-cell time-lapse images of WT (L) or PIP5K1C-GFP overexpressing (M) RAWA 264.7 macrophage cells responding to global simulation with 1 μM of C5aR agonist. Cytosol to membrane translocation of PHAkt-mCherry was monitored over time. Time in min:sec format and C5aR agonist was added at time $t = 0$. **N** Normalized responses shown by WT (gray) and PIP5K1C-GFP overexpressing (mint green) RAW 264.7 cells to different doses of C5aR agonist. Responses are expressed as (1 - minus decrease in cytosolic intensity of PHAkt-mCherry). Here, nc ≥ 14 cells for each concentration, for either population, from $N \geq 3$ independent experiments. The *p* values are computed by the two-tailed Mann−Whitney U test. **O, P** Live-cell time-lapse images (**O**) and quantification of the level of newly-polymerized F-actin (**P**) in *Gβ− Dictyostelium* cells co-expressing Dox-inducible PIP5K-GFP and LimE-mCherry, without or with overnight Dox induction. In (**P**), $n_c = 20$ for either condition from $N \geq 3$ independent experiments; *p* value by two-tailed Mann−Whitney U test.

differentiated HL-60 macrophages led to a very flat, rounded phenotype and abolished protrusions (Supplementary Fig. 10A–F and Supplementary Movie 14). Third, in mouse primary CD8 + T cells, like neutrophils, low-expressing cells were polarized, with PIP5K1C at the rear (Fig. 1I), while high-expressing cells were rounded and immobile (Supplementary Fig. 10G–J).

Next, we extended our inquiry to epithelial-derived cancer cells by studying MDA-MB-231 cells. In scratch-wound closing assays (Supplementary Fig. 11A), cells overexpressing PIP5K1C were rounded, and the speed of closing the wound was significantly delayed (Fig. 2M, N and Supplementary Fig. 11B). Strikingly, overexpressing PIP5K1C prevented the dissociation of cells from 3D spheroids, cells were rounded but remained attached in the center of the spheroid and did not disseminate for over 48 h (Fig. 2O–Q and Supplementary Fig. 11C–E).

Overexpressing PIP5Ks suppresses signal transduction and cytoskeletal activities

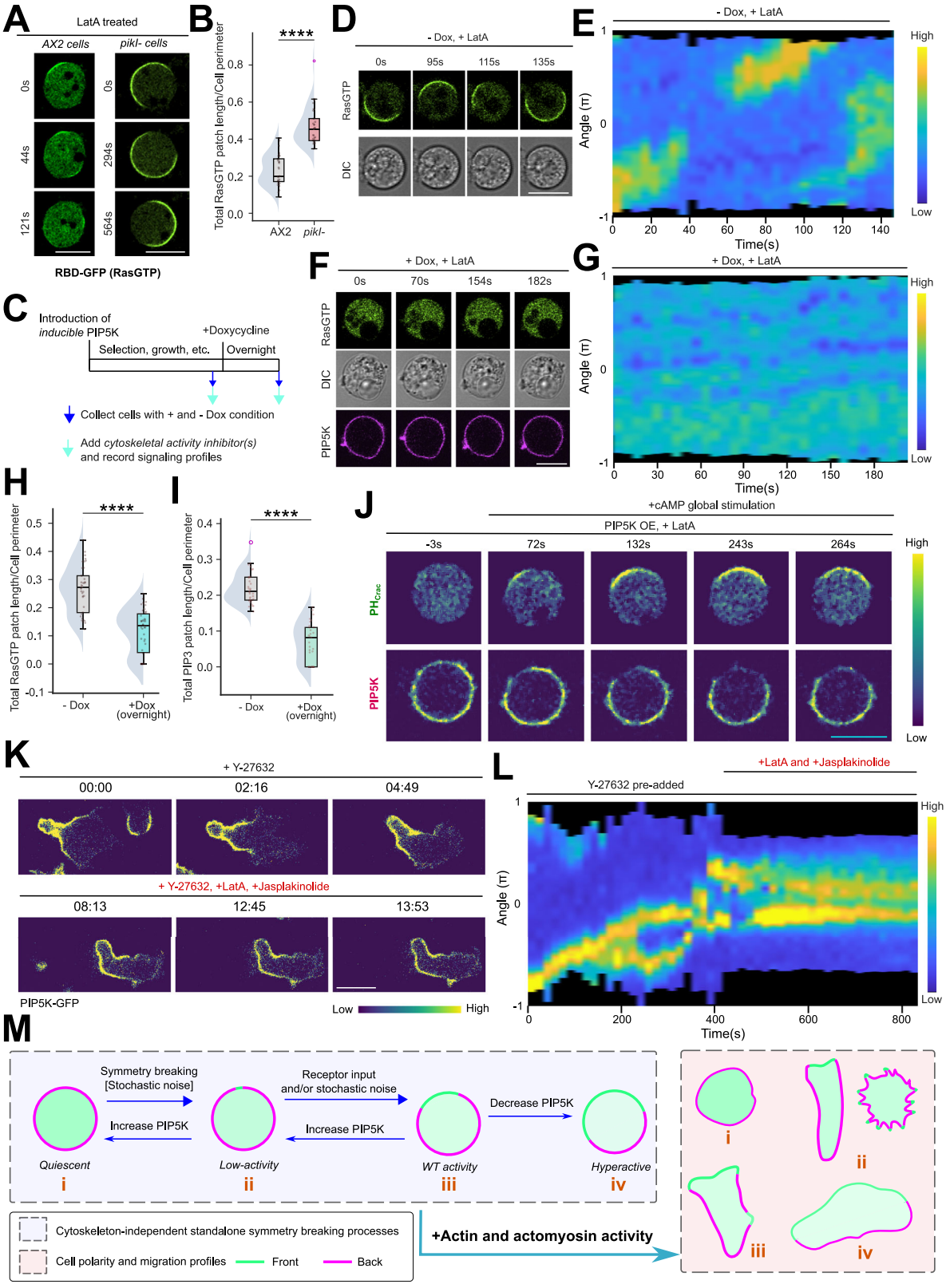
To dissect how PIP5K levels modulate different feedback loops, we examined the profiles of a series of signal transduction and cytoskeletal activities using biosensors. An abridged version of the biochemical network controlling cell migration is illustrated in Fig. 2R. We observed the spatial distribution of Ras activity in *Dictyostelium* cells with different Dox incubation times. Without Dox incubation, cells showed characteristic RBD patches at the cell protrusions (Fig. 3A and Supplementary Movie 15), whereas cells incubated with Dox overnight had substantially inhibited Ras activity. There were almost no RBD patches in rounded, non-moving cells (Fig. 3B, Supplementary Movie 15), whereas in the spiky cells, there were tiny patches (Supplementary Fig. 12A–D and Supplementary Movie 15). Combining data from rounded and spiky cells, there was an overall 65% reduction in total Ras patch length (Fig. 3C). Without Dox, cells displayed broad, sustained waves of RBD on their ventral surface; following overnight Dox, cells showed either no waves or smaller, slower-moving waves (Fig. 3D and Supplementary Movie 16). Since rounded cells did not exhibit any membrane patches, in S12B and subsequent figures, we quantified spiky cells only as a conservative measure of the inhibitions. Similar results were observed when we examined PIP3 and cytoskeletal activities in cells (Fig. 3E–J, Supplementary Fig. 12E–H, and Supplementary Movie 16). The dynamic behavior was captured in t-stack kymographs (Fig. 3K), indicating that the tiny F-actin patches in cells expressing PIP5K are more transient than patches in untreated cells. Examination of the ArpC biosensor was consistent with the F-actin results (Supplementary Fig. 13A, B). We also used a Pak1-GBD biosensor to examine Rac1 activity. The Rac1 activity resembled F-actin (Supplementary Fig. 13C–F). Additionally, we examined Ras, PIP3, and cytoskeletal activities in cells incubated with Dox for only 2 h or in cells expressing mutant PIP5K (K681N and K682N), which were more polarized and migrated more rapidly. We found that all these activities were confined to tiny patches at the leading edge or undetectable (Supplementary Fig. 13G–J and Supplementary Movie 17).

We next examined interactions between PIP5K and other signaling components. First, we have previously reported that cells lacking G-actin-sequestering actobindins A, B, C (*abnABC*- cells) have increased Ras and PI3K activity, suggesting that branched actin is in a positive feedback loop with these signal transduction activities[81]. We examined how strongly PIP5K inhibition can interrupt this feedback loop by overexpressing the enzyme in *abnABC*- cells. Without Dox incubation, cells showed broad RBD patches as expected (Supplementary Fig. 14A and Supplementary Movie 18). Upon overnight Dox incubation, the RBD patches decreased in length and increased in number (Supplementary Fig. 14B and Supplementary Movie 18), indicating competition between the positive feedback from branched actin and inhibition by PIP5K. Second, we previously reported that a RasGAP, C2GAPB, in *Dictyostelium* cells can inhibit Ras activities and increase polarity and migration speed (Supplementary Fig. 14C)[60]. Since *pikI*- cells have much higher Ras activity, we tested whether attenuating Ras activity in these cells could restore polarity and migration (Supplementary Fig. 14C). Indeed, upon overexpressing C2GAPB, the *pikI*- cells changed from fan-shaped or oscillatory cells to more polarized cells, with migration speed exceeding that of either (Supplementary Fig. 14D–F and Supplementary Movie 19). In contrast, co-expressing PIP5K and C2GAPB completely shut down migration, presumably due to severe Ras deactivation (Supplementary Fig. 14G and Supplementary Movie 19).

As overexpressing PIP5Ks in HL-60 neutrophils showed migration and morphological phenotypes like those of *Dictyostelium* cells, we tested whether the effects on signaling networks are also conserved. As previously reported[18,24,47,82,83], PIP3 and F-actin preferentially localized to the leading edge of migrating neutrophils (Supplementary Fig. 15A, B). In rounded neutrophils overexpressing PIP5K, F-actin activities were greatly diminished (Supplementary Fig. 15C, D). Even in the polarized populations expressing PIP5K, PIP3 activities remained low (Supplementary Fig. 15E, F). Thus, the inhibition of signal transduction and cytoskeletal activities by PIP5K expression is a shared phenomenon.

The reduced spontaneous signaling and curtailed wave activity seen in PIP5K-overexpressing cells indicate that the threshold of the

https://doi.org/10.1038/s41467-026-77894-2



excitable network is increased[16]. To more directly assess the threshold, we tested how the enzyme level interferes with receptor input-driven activities. We first monitored the profile of PIP3 biosensor PH_{Akt} upon C5aR activation in RAW 264.7 macrophages[26,84]. When cells were stimulated with 1 μM C5aR agonist, PH_{Akt} transiently translocated to the membrane and cells extended protrusions (Fig. 3L and Supplementary Movie 20). In contrast, at this concentration, there was little or no PIP3 increase or protrusion formation in cells overexpressing PIP5K1C (Fig. 3M, Supplementary Movie 20), and there was only a moderate increase at 100 μM C5aR agonist (Supplementary Fig. 16A–G and Supplementary Movie 20). Compared with WT cells, the dose-response spanning 0.1 μM to 100 μM C5aR for PIP5K1C-expressing

Fig. 4 | Mutually inhibitory actions of Ras-PIP5K can function in the absence of cytoskeletal dynamics. A Live-cell images of WT AX2 (left) and *pikI-* (right) *Dictyostelium* cells expressing RBD-GFP, pre-treated with Latrunculin A (5 μM) and caffeine (4 mM). **B** Quantification of overall RasGTP level on the cell membrane in AX2 or *pikI- Dictyostelium* cells after Latrunculin A treatment. The levels are expressed as total RBD-GFP patch length per unit perimeter length. Here, $n_c = 33$ for AX2 populations, and $n_c = 29$ for *pikI-* cells populations. The p-values are computed by the two-tailed Mann–Whitney U test. **C** Schematic of the experimental strategy involving Dox-inducible promoter-driven PIP5K overexpression, followed by inhibition of cytoskeletal activities. **D, F** Live-cell images of *Dictyostelium* cells co-expressing RBD-GFP and Dox-inducible mRFP-PIP5K without (**D**) or with overnight Dox induction (**F**). Cells were pre-treated with Latrunculin A (5 μM) and caffeine (4 mM). **E, G** Representative 360° membrane kymograph of RBD-GFP, corresponding to Fig. 4D, F, respectively. **H, I** Quantifications of overall RasGTP level (**H**) or PIP3 level (**I**) on the cell membrane in *Dictyostelium* cells with Dox-inducible PIP5K overexpression system, without or with Dox induction. The levels are expressed as total RBD-GFP patch length (**H**) or PHcrac-YFP patch length (**I**) per unit perimeter length. Here, $n_c = 37$ (**H**, −Dox overnight), 46 (**H**, +Dox overnight), 35 (**I**, −Dox overnight), or 29 (**I**, +Dox overnight) cells. The *p* values are computed by the two-tailed Mann–Whitney U test. **J** Live-cell images of *Dictyostelium* cells co-expressing PHcrac-RFP and Dox-inducible GFP-PIP5K with overnight Dox induction. Cells were pre-treated with Latrunculin A (5 μM) and caffeine (4 mM) and then stimulated with 5 μM cAMP at $t = 0$. **K** Live-cell images of differentiated HL-60 neutrophils expressing GFP-PIP5K. Cells were treated with 5 μM ROCK inhibitor Y-27632, followed by 8 μM Jasplakinolide and 5 μM latrunculin B. Time in min:s format. **L** Representative 360° membrane kymograph (see "Methods" for details) of GFP-PIP5K in differentiated HL-60 neutrophils, corresponding to Fig. 4K. Inhibitors were added as indicated on top. **M** Schematic showing different signaling states (blue box) and corresponding cellular morphologies (salmon box) in the absence or presence of cytoskeletal activities. The notations "i"–"iv" denotes the correspondence. Note that, increase and decrease in PIP5K level in cell can enable transition among signaling states and when cytoskeleton is engaged, it can regulate the cell migration mode, polarity, and morphologies.

cells was shifted to higher concentrations (Fig. 3N). Similar results were observed when we monitored Ras-GTP profiles upon folic acid (FA) stimulation in WT versus PIP5K overexpressing *Dictyostelium* cells (Supplementary Fig. 17A–D). To test whether the increases in threshold in these cases were due to the effects on the receptor activity or affinity, or intrinsic to the excitable network, we used *Dictyostelium* cells lacking the only Gβ subunit. Although these cells are unable to respond to chemoattractant[19,85,86], the effects of PIP5K overexpression on spontaneous activity could be assessed. Indeed, spontaneous F-actin activities were strongly inhibited (Fig. 3O–P and Supplementary Movie 21). Considering that F-actin is a "downstream" indicator of network activity, these data indicate the inhibitory effect of PIP5K is exerted directly within the excitable network.

Abrupt perturbation of membrane PIP5K level can regulate symmetry breaking and protrusion formation

To directly test the immediate effects of altering the association of PIP5K with the membrane and rule out secondary factors, such as changes in transcriptional or proteomic profiles, we designed optogenetic systems to rapidly remove PIP5K from the membrane or recruit a cytosolic version to the membrane. First, we tested whether the quiescent phenotype induced by PIP5K overexpression in RAW 264.7 macrophages can be reversed by removal of the enzyme from the membrane. We engineered the Opto-SeqP system to rapidly sequester the overexpressed PIP5K from the membrane to mitochondria (Supplementary Fig. 18A). Upon blue light illumination in macrophages with Opto-SeqP, membrane PIP5K levels quickly decreased, and cells began to make many small protrusions (Supplementary Fig. 18B–E and Supplementary Movie 22). These protrusions often eventually resulted in an elongated cell shape (Supplementary Fig. 18B, C and Supplementary Movie 22). Quantification shows that blue light illumination significantly increased protrusion formation frequencies in cells with Opto-SeqP, whereas recruiting a control construct to mitochondria did not elicit any changes (Supplementary Fig. 18F–I and Supplementary Movie 22).

Next, to test if rapidly increasing PIP5K level on the membrane would inhibit receptor-mediated protrusions, we engineered the Opto-RecP system based on a previously reported cytosolic, functional version of PIP5K[87] (Supplementary Fig. 19A). We recruited either cytosolic PIP5K or a cytosolic control construct to the membrane of RAW 264.7 macrophages and then stimulated them with a C5aR agonist. Compared with the control recruitment, where C5aR stimulation induced large protrusions and strong cell spreading[25,84,88], recruitment of the cytosolic PIP5K completely blocked the response, and cells remained quiescent (Supplementary Fig. 19B–F and Supplementary Movie 23). Furthermore, globally recruiting cytosolic PIP5K to the plasma membrane in MDA-MB-231 cells (pretreated with saturating doses of EGF) induced cell retraction (Supplementary Fig. 20A–E, H, I and Supplementary Movie 24), whereas recruiting the control did not alter cell area or aspect ratio (Supplementary Fig. 20F, G, J, K and Supplementary Movie 24). Taken together, these observations demonstrate that in this context, the acute perturbation of the membrane PIP5K level is necessary and sufficient to regulate protrusion formation events, and these effects are not mediated via the long-term changes in transcriptional or proteomic profiles.

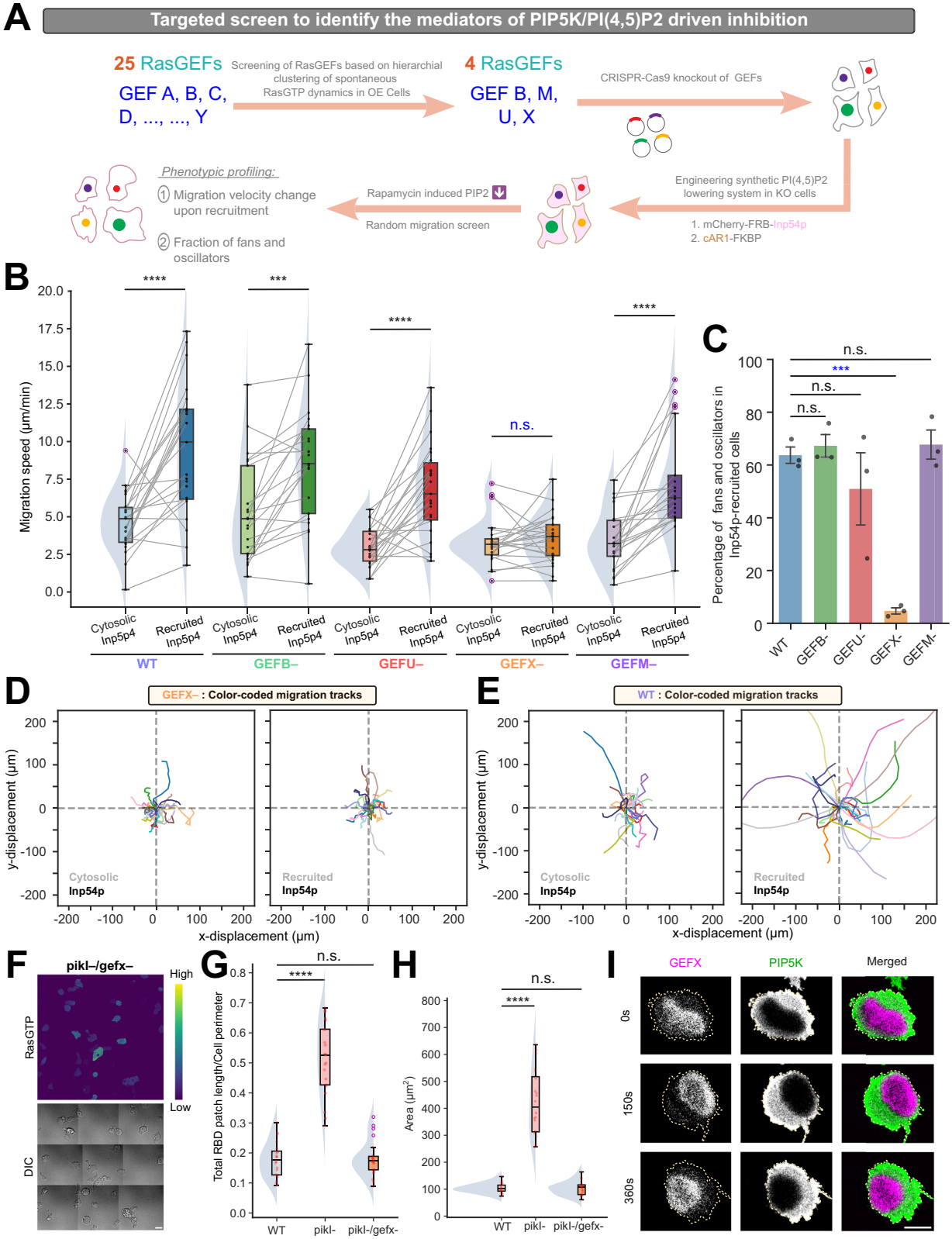
Inhibiting actomyosin contractility counteracts PIP5K overexpression-induced phenotypes

In previous experiments (Fig. 3), we showed that expressing PIP5Ks can eliminate signal transduction, cytoskeletal activities, and cell migration. We hypothesized that under normal conditions, the inhibitory effects of PIP5Ks would be reinforced by actomyosin-based inhibitory feedback loops. To test the extent to which reducing the negative feedback by lowering Myosin II would counteract PIP5K expression and restore migration, we co-expressed PIP5K and a recruitable myosin heavy chain kinase C (MHCKC) that was previously shown to abruptly decrease myosin II bipolar thick filament assembly[81] (Supplementary Fig. 21A, B and Supplementary Movie 25). Remarkably, in PIP5K overexpressing cells, global recruitment of MHCKC to the plasma membrane caused immobile cells to polarize and migrate (Supplementary Fig. 21C–F and Supplementary Movie 25). Consistently, while PIP5K expression completely suppressed propagating waves of Ras activity, adding the Myosin II inhibitor, blebbistatin, reignited a burst of waves that gradually spread across the entire surface (Supplementary Fig. 21G and Supplementary Movie 26).

A bistable Ras–PIP5K interaction mediates the symmetry breaking independent of cytoskeletal dynamics

To determine whether the role of Ras-PIP5K interaction in symmetry breaking requires cytoskeletal activity, we treated cells with different PIP5K levels with cytoskeletal inhibitors. We first treated WT and *pikI- Dictyostelium* cells with Latrunculin A to remove F-actin activities and caffeine to enhance oscillatory wave dynamics[14]. We monitored patches of RBD, which appear as dynamic crescents moving around the cell perimeter. Consistent with the large patches seen in *pikI-* cells with intact cytoskeletal dynamics, the Ras activity crescents were much wider than in WT cells but maintained some dynamics (Fig. 4A, B and Supplementary Movie 27). To test whether the inhibitory effects of PIP5K expression depended on the cytoskeletal activity, we examined Latrunculin A-treated PIP5K overexpressing cells under the conditions that produce the rotating Ras and PIP3 crescents and observed that the

https://doi.org/10.1038/s41467-026-77894-2



crescents were severely diminished (Fig. 4C–I, Supplementary Fig. 22A–D, and Supplementary Movie 27).

We next asked whether the localization of PIP5K depends on cytoskeletal activity. First, we used the low-level expression system and a uniform cAMP stimulus to observe PIP5K localization with respect to the typical oscillatory crescents of PIP3. In Latrunculin A-treated cells, PIP5K was dynamically depleted from "front" membrane domains marked by the PIP3 biosensor (Fig. 4J and Supplementary Fig. 22E). Second, we examined PIP5K in "stalled" neutrophils that maintain a polarized form in the absence of cytoskeletal dynamics when treated with a cocktail of Jasplakinolide, Latrunculin B, and ROCK inhibitor Y-27632 (JLY)[24,89]. It has been puzzling how these immobile cells, with

Fig. 5 | Genetic screen in *Dictyostelium* identifies that PIP5K/PI(4,5)P2 inhibits Ras activation on the plasma membrane by regulating RasGEFX profile. **A** Schematic showing the workflow of targeted genetic screen to identify the RasGEFs that activate Ras in response to a decrease in PI(4,5)P2. First, four GEFs were selected from the list of 25. Next, a chemically inducible dimerization for synthetic PI(4,5)P2 lowering (see Methods) was incorporated in the cells where one of these 4 GEFs were deleted. Finally, cell migration was profiled in these cells, before and after rapamycin induced acute PI(4,5)P2 lowering. **B** Quantification of average migration speed of wild-type AX2, *gefB*-, *gefU*-, *gefX*-, and *gefM*- cells, before and after rapamycin induced PI(4,5)P2 lowering. Here, $n_c = 23$ (WT), 21(*gefB*-), 23 (*gefU*-), 25 (*gefX*-), 22 (*gefM*-) cells and each cell has been tracked for $t = 22$ min for before and after recruitment. For pairwise comparison between before and after recruitment, data from the same cell are connected by gray lines; the p values are computed by the two-tailed Wilcoxon signed-rank test. **C** Quantification of percentage of cells migrating as fans and oscillators after PI(4,5)P2 lowering in wild-type AX2 and RasGEF knock out cell populations. Each data point indicates one independent experiment where at least 40 cells were profiled. The p values by two-tailed welch t-test. Error bars: SEM. **D, E** Centroid tracks of migrating *gefX*- (**D**) and wild-type AX2 (**E**) cells, before and after PI(4,5)P2 lowering. For pairwise comparison, tracks from the same cell are plotted in same color in before and after recruitment populations. Here, $n_c = 25$ (*gefX*-) and 23 (AX2) cells and each cell has been tracked for $t = 22$ min for before and after recruitment. All the tracks were reset to the same origin. **F–H** Representative live-cell image of *gefX-/pikI−* cells expressing RBD-GFP. Note absence of hyperactivated Ras signaling or fan/oscillator like morphology. **I** Ventral wave propagation in cells co-expressing mCherry-RasGEFX and GFP-PIP5K. Note that, RasGEFX and PIP5K maintain consistent complementarity as waves propagate.

actin turnover and myosin-based contractility halted, maintain polarized sensitivity to receptor stimulation[24]. Remarkably, we found that PIP5K persistently maintained a strong back localization in JLY-treated neutrophils (Fig. 4K, L, Supplementary Fig. 22F, G, and Supplementary Movie 28). Given our evidence that PIP5K is a negative regulator of Ras activity and other signal transduction activity, its persistent back localization can explain the reduced sensitivity at the back.

Our data so far indicate that the inherent Ras-PIP5K antagonism is critical for symmetry breaking on the plasma membrane (Fig. 4M). In an initially quiescent cell, PIP5K is uniformly distributed on the membrane. Ras and other signaling activities are absent. We propose that stochastic noise turns on "sparks" of Ras signaling[90] or depletion of PIP5K on a local membrane domain, which initiates positive feedback. This mutually inhibitory positive feedback loop amplifies the initial event and the spread of activities. Increasing or decreasing PIP5K levels can vastly inhibit or activate Ras accordingly (Fig. 4M). When connected to other signaling and cytoskeletal pathways, this core circuit can tune polarity and, thereby, generate distinct morphological states and migratory modes, as we have observed (Figs. 1 and 2).

RasGEFX mediates PIP5K/PI(4,5)P2 driven inhibition of Ras activation

Our results have demonstrated the central role of RasGTP-PIP5K mutual inhibition, but it remains unclear how PIP5K/PI(4,5)P2 inhibits RasGTP. To address this question, we speculated that specific RasGEFs are inhibited by high PIP5K/PI(4,5)P2 levels and that deletion of one or more of these GEFs would subvert the phenotype induced by lowering PI(4,5)P2. To test this idea, we focused on RasGEFs B, M, X, and U, which we previously found to enhance spontaneous Ras activity[27]. Reasoning that one or more of these GEFs mediate the regulation of Ras activity by PIP5K/PI(4,5)P2, we focused our screen on them.

We first expressed a chemically inducible dimerization-based synthetic PI(4,5)P2 depletion system in cells lacking each of these RasGEFs and observed random migration before and after rapamycin-driven acute PI(4,5)P2 depletion (Fig. 5A). In WT cells, decreasing PI(4,5)P2 significantly increased cell migration speed, and a majority of cells switched their migration mode to fans and oscillators (Fig. 5B, C), as reported previously[16,17]. Strikingly, in *gefX*- cells the effects of lowering PI(4,5)P2 were nearly abolished (Fig. 5D, E). There was a slight effect in *gefB*- cells, whereas the phenotypic changes caused by PI(4,5)P2 lowering were negligible in *gefM*- and *gefU*- cells (Fig. 5B, C and Supplementary Fig. 23A–C). To further investigate the interaction between PIP5K and RasGEFX, we generated *pikI-/gefX*- cells and examined the Ras activities in these cells. Remarkably, in these cells, the cell area, migration speed, and Ras activity patches reverted towards WT levels (Fig. 5F–H, Supplementary Fig. 23D, E, and Supplementary Movie 29). This suggests that the Ras-PI(4,5)P2 circuit can be restored to a balanced state and function again at lower levels of both key components.

These results push the regulatory circuit back a level to mutual inhibition between PI(4,5)P2 and RasGEFX. Consistently, expressing RasGEFX in normally quiescent PIP5K-overexpressing cells led to wide undulations of the cell boundary (Fig. 5I, Video S30). These were correlated with ventral wave propagation, which does not occur in cells overexpressing PIP5K alone. Furthermore, in the cells expressing PIP5K and RasGEFX, the two proteins maintained consistent complementarity (Fig. 5I and Supplementary Video 30). Taken together, our data further document a mutual inhibitory interaction between RasGEFX and PIP5K, where each protein, directly or indirectly, controls the localization of the other.

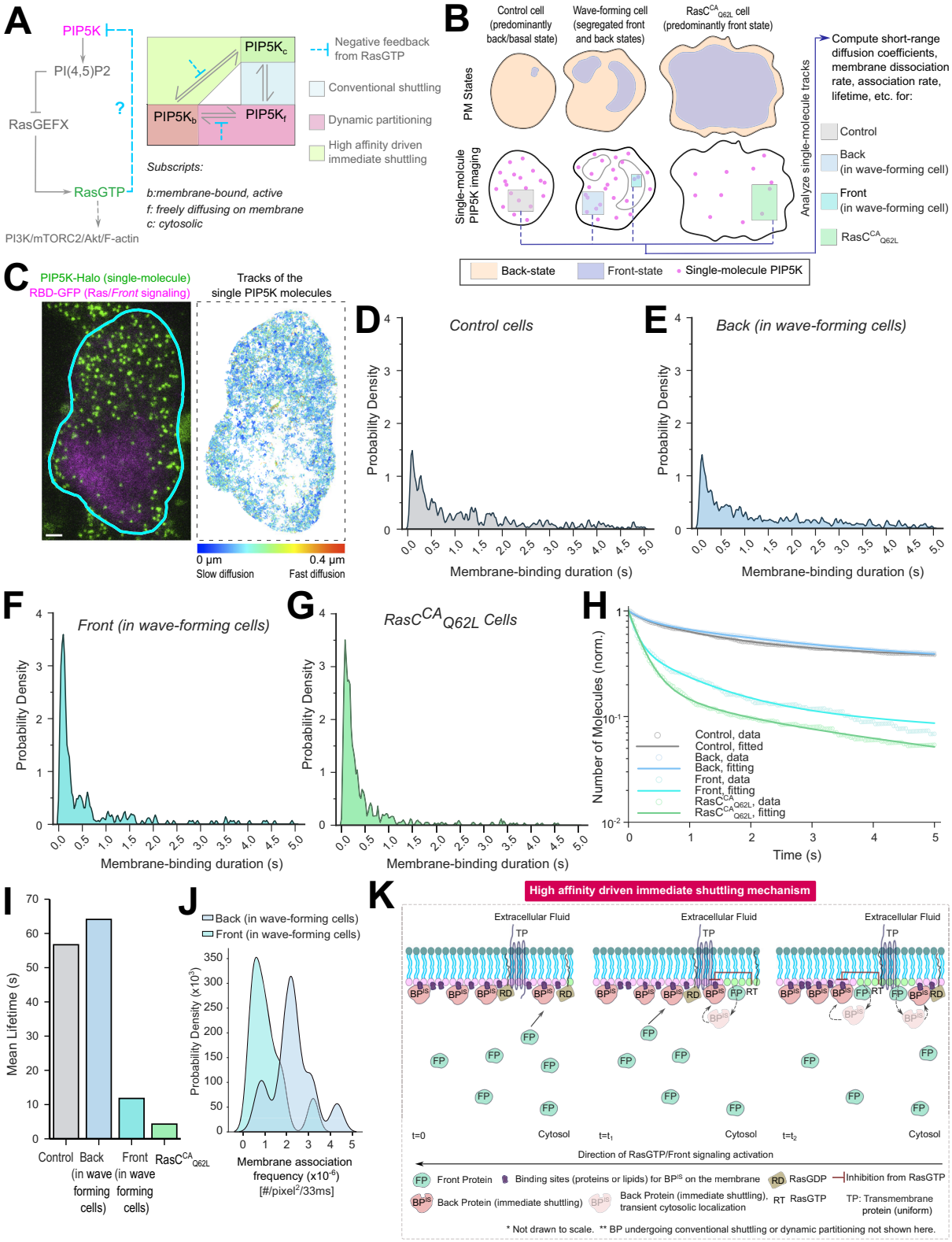
Single-molecule measurements show activated Ras increases dissociation rate of PIP5K from the membrane

Next, we investigated how Ras regulates PIP5K localization (Fig. 6A). Activated Ras could increase PIP5K diffusion within the membrane or promote its dissociation into the cytosol[13,26] (Supplementary Fig. 24A, B). In response to global stimulation, "shuttling" proteins translocate to the cytosol, whereas proteins that compartmentalize through differential membrane diffusion, a process termed "dynamic partitioning," remain membrane-associated[26] (Supplementary Fig. 25A). We observed neither significant PIP5K translocation to the cytosol upon stimulation nor the appearance of photoconverted membrane PIP5K in the cytosol, initially suggesting that PIP5K may relocate by dynamic partitioning rather than shuttling (Supplementary Fig. 25B–F; see also Supplementary Figs. 16 and 17 for PIP5K dynamics during global receptor activation in different systems; Supplementary Movies 31 and 32).

To test whether PIP5K diffuses heterogeneously in the front and back state regions of the membrane, we designed a multiscale imaging regime where we tracked front state membrane domains using a RasGTP biosensor and tracked single-molecule diffusion of PIP5K on the other channel[91]. We tracked diffusion in quiescent, wave-forming, or $RasC_{Q62L}$ expressing cells, which have increasingly more Ras activities (Fig. 6B). PIP5K-Halo was observed as diffusive fluorescent spots (Supplementary Fig. 26A). Single-step photobleaching patterns and the distribution of fluorescence intensities verified that the fluorescent spots of PIP5K-Halo-TMR represent single molecules (Supplementary Fig. 26 and Supplementary Movie 33). We measured the movement of individual PIP5K molecules in both the front- and back-state regions of the membrane using single-molecule tracking (Fig. 6C). Surprisingly, the short-range diffusion coefficient of PIP5K was not substantially different between front and back states of the membrane, and furthermore, was slightly slower in $RasC_{Q62L}$ expressing cells (Supplementary Fig. 27A–H), questioning our dynamic partitioning hypothesis.

Next, we measured the lifetime of PIP5K molecules under the same experimental conditions. The lifetime in the front state regions and $RasC_{Q62L}$ expressing cells was significantly shorter than in back state regions or in quiescent cells (Fig. 6D–I). Furthermore, the

https://doi.org/10.1038/s41467-026-77894-2



membrane association frequency of PIP5K in back-state regions was nearly three times higher than in front-state regions (Fig. 6J). Consistently, a detectable amount of PIP5K was moved to the cytosol of cells expressing RasC$_{Q62L}$ (Supplementary Fig. 27I). Taken together, these data suggest that the dissociation constant in activated front-state regions are nearly two orders of magnitude larger than in back-state regions. This difference can explain the depletion of molecules at the front and enrichment at the back and suggests that PIP5K molecules dynamically dissociate from front-state regions and bind to back-state regions (Fig. 6K, also see Fig. 1). The affinity of PIP5K molecules for the membrane must be extremely high, or there must be a large excess of binding sites on the membrane since so little enzyme is found in the cytosol as these relocations occur under normal physiological circumstances.

Fig. 6 | Single-molecule Imaging of PIP5K in *Dictyostelium* reveals RasGTP increases the dissociation constant for PIP5K membrane binding. A Left: Schematic of the core signaling network that triggers plasma membrane symmetry breaking and engages with downstream PI3K/mTORC2/Akt/F-actin network to properly polarize cell and generate localize protrusions. The nature of the blue inhibitoryfeedback loop(blue) is incompletely known. Right: The possible states that PIP5K can assume in the membrane and cytosol are shown, along with the potential mechanisms by which PIP5K activity on the membrane can be limited. For details on conventional shuttling and dynamic partitioning, please see Supplementary Fig. 24 and Banerjee et al. 2023. The high affinity shuttling mechanism is delineated in Fig. 6k. Blue inhibitory loop, consisting of actions from RasGTP driven negative feedback to PIP5K, can potentially act in different ways, as shown here. **B** Illustration of the multiscale imaging setup where PIP5K-Halo (TMR conjugated) is tracked at the single-molecule level while front signaling state regions on the membranes are tracked with RBD-GFP during ventral wave propagation. The assay was performed in conditions where Ras is increasingly more activated, such as basal/quiescent cells (membrane predominantly back-state), cells with propagating waves (where membrane dynamically segregates into front and back state regions), and cells with constitutively active Ras (where is membrane is largely in front or activated state). From these conditions, short-range diffusion coefficients, lifetimes, membrane association and dissociation rates were computed for four different categories of membrane domains, as shown in the figure. **C** Left: Representative live-cell multiscale TIRF microscopy image of a *Dictyostelium* cell, where magenta shows the demarcated front signaling regions and green shows individual PIP5K-Halo-TMR molecules. Cell boundary is shown with the cyan outline. Right: The trajectories of single PIP5K molecules motion detected during 4 s from the cell shown in left. The colormap below indicates the amount of diffusion. Scale bar indicates 2 μm. **D**–**G** Kernel density estimation plots showing the probability density distribution of the membrane-binding durations of PIP5K in four different categories of membrane domains as shown in (B): quiescent cells (**D**), back-stateregion in wave-forming cells (**E**), front-stateregion in wave-forming cells (**F**), and cells with constitutively active Ras (**G**). For all of these plots, scott was used as the bandwidth method and bw_adjust = 0.04 was used to maintain consistent scaling. Note that, substantially more PIP5K molecules dissociate from the membrane domains as Ras activation increases. **H** Temporal profile of dissociation of PIP5K molecules from four categories of membrane domains (as depicted in (**B**)), demonstrating that the dissociation rate of PIP5K molecules from membrane increases as Ras gets increasingly more active. Means are shown and lines represent the fitted data. **I** Mean lifetimes of PIP5K in four categories of membrane domains (as depicted in (**B**)). **J** Kernel density estimation plots showing the probability density distribution of the membrane association of PIP5K in back vs front state regions in cells, demonstrating PIP5K molecules bind more effectively to the back-state, compared to the front-state. Here scott was used as the bandwidth method and bw_adjust = 0.5 was used. **K** Schematic showing the suggested high affinity shuttling mechanism. Lipid headgroups associated with the back-state and front-state are shown in mauve color and green color, respectively. At $t = 0$, the membrane is in complete back-state. A wave of signaling activation initiated at the right is shown propagating to the left at t=0, t1, and t2. As wave propagates and Ras switches from GDP to GTP bound state in specific membrane domains, front proteins translocate to those membrane domains from the cytosol. Simultaneously, in those domains, RasGTP alters membrane binding of BP^{IS} (PIP5K molecule), prompting its translocation to cytosol. Due to a saturating amount of binding sites (shown in dark violet), dissociated BP^{IS} molecules immediately bind to other parts of the membrane. Thus, RasGTP maintains complementarity with PIP5K Mechanismis distinct from conventional shuttling, where there is a significant cytosolic pool, and dynamic partitioning, where molecules do not leave the membrane. TP molecules are shown as fixed, fiducial component. Solid arrows are shuttling between the membrane and cytosol and the dashed arrows are showing transient immediate shuttling.

The stochastic, reaction-diffusion model explains PIP5K-driven tuning of signaling activities

Figure 7 summarizes the molecular interactions that we propose to account for excitability, signal amplification, symmetry breaking, and polarity establishment. The core of the network consists of the mutual inhibition between PI(4,5)P2 and RasGTP. PI(4,5)P2 inhibits Ras activation, and in turn, activated Ras lowers PI(4,5)P2 by increasing PIP5K dissociation from the membrane. Importantly, the total amount of PIP5K on the membrane is relatively constant such that enzyme leaving one region accumulates elsewhere. The mutual antagonism creates an effective positive feedback loop which, in conjunction with delayed negative feedback from PIP3/Akt, confers biochemical excitability to the core loop. These events can occur independently of cytoskeletal activities. However, under normal physiological conditions, PIP3/Akt favors branched actin over linear acto-myosin, which feeds back positively to Ras. Increased PI(4,5)P2 may also promote acto-myosin, contributing to Ras inhibition.

To assess the feasibility of these schemes in silico, we developed a mathematical model that combines the key molecular interactions with a level-set framework, which simulates cell boundary movement[16,92,93]. The model was built iteratively with experimental data and is intended as a mechanistic framework rather than a post hoc fit; its value lies in showing that manipulation of the core Ras-PIP5K circuit is sufficient to generate the observed behaviors. In WT conditions, stochastic noise triggers transient Ras activation (Fig. 7), which spreads as V-shaped waves in kymographs. PIP5K and PI(4,5)P2 are depleted from those areas, whereas PIP3/Akt follows them (Fig. 7 and Supplementary Fig. 28A–D). Consequently, branched actin appears in the regions where Ras is activated, and actomyosin is depleted (Supplementary Fig. 28A–D). When PIP5K is overexpressed, Ras and branched actin are confined to small patches or extinguished, and the entire cortex is shifted toward the back state. When PIP5K activity is absent and/or PI(4,5)P2 is depleted, Ras is highly activated, and, once triggered, signal transduction events and branched actin spread across most of the cortex and oscillate. With increased polarity, the signaling remains on across only half of the cell. When the feedback loops from actin and myosin are removed, the core network can still break symmetry and remains excitable (Supplementary Fig. 29A–K). Even when PIP5K is deleted, remaining PI(4,5)P2 can likely maintain excitability as long as Ras activity is also low (Supplementary Fig. 29L–N).

To visualize the effects of these perturbations on cell migration, we developed a system in which the output, represented by PIP3/Akt and branched actin activity, drove the expansion of a viscoelastic boundary. As shown in Fig. 7H and Supplementary Movie 34, in WT cells, each wave of Ras activation creates a bilateral protrusion with a cup-like morphology. The cup is formed because, as evidenced by the kymograph, activation occurs at the spreading tips, while inhibition follows. When PIP5K is high, protrusions become smaller or disappear entirely and cells stop migrating. When PIP5K is absent, PI(4,5)P2 levels are low, protrusions are wide, and cells switch their migratory behaviors from amoeboid to oscillatory or fan-shaped phenotypes.

Discussion

Figure 8 illustrates the network in greater detail, highlighting the molecular interactions that we propose to account for symmetry breaking and signal amplification, ultimately leading to the establishment of polarity. Within the core circuit (see shaded box), reduced levels of PI(4,5)P2 activate Ras by promoting recruitment of RasGEF to the membrane. Activated Ras increases the dissociation rate of PIP5K from the membrane, thereby lowering PI(4,5)P2 and completing a positive feedback loop. Crucially, dissociated PIP5K molecules rapidly bind to other regions of the membrane, clamping PI(4,5)P2 levels and thereby preventing RasGEFX from accessing the membrane, activating Ras and initiating a new cycle there. Beyond this, activated Ras couples to the PI3K/mTORC2/Akt pathway, triggering branched actin polymerization and inhibiting myosin assembly, while increased PI(4,5)P2 promotes linear actomyosin. Branched and linear actin provide positive and negative feedback loops to Ras, respectively. As shown in Fig. 8B, in the basal state, PIP5K is on the membrane, PI(4,5)P2 levels are high, RasGEFX is in the cytosol, Ras-GTP activity is low, and the cell

https://doi.org/10.1038/s41467-026-77894-2

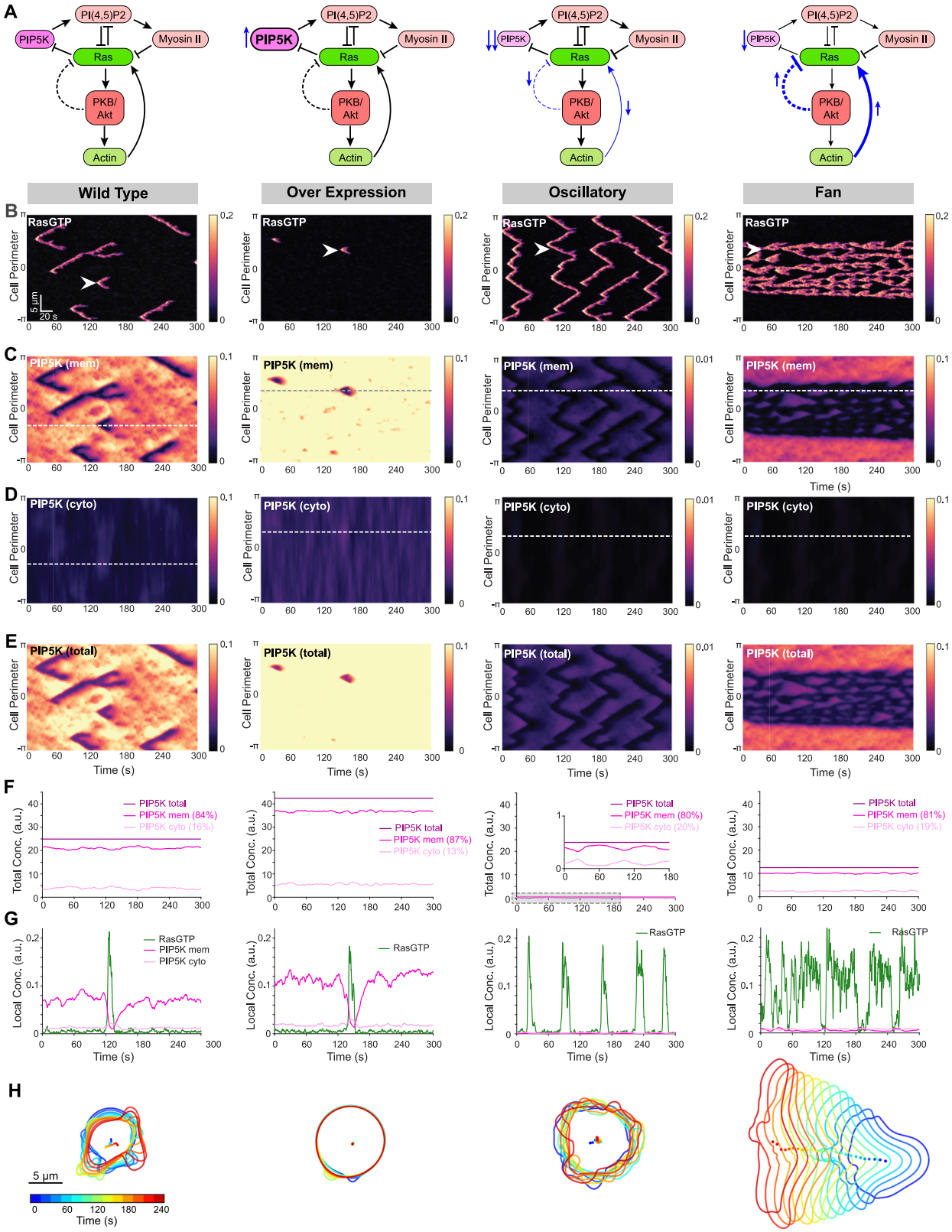


Fig. 7 | A stochastic reaction-diffusion model recreates experimental observations. A Schematic illustrating the key signaling interactions included in the model. Phenotype-dependent changes in species concentration and feedback strength are indicated by line thickness and color. The dashed line denotes the actin-mediated global negative feedback on Ras. **B**–**E** Kymographs of molecular dynamics over a 300 s simulation: **B** Ras, **C** membrane-associated PIP5K, **D** cytosolic PIP5K, **E** total PIP5K. Columns correspond to different conditions: wild type (1st), PIP5K overexpression (2nd), piki- oscillatory phenotype (3rd), and fan phenotype (4th). **F** Time series of total PIP5K (dark purple), membrane-associated (purple), and cytosolic (light purple) fractions, summed across the cell perimeter. Total PIP5K remains conserved over time, but differs across phenotypes, mimicking the experimental manipulations. **G** Local concentration profiles of Ras (green), membrane-associated (purple), and cytosolic (light purple) PIP5K at the spatial location marked by the arrow in (**B**) and dashed lines in (**C**, **D**). These dynamics highlight a causal relationship: Ras activation correlates with decreased membrane association and a transient increase in cytosolic PIP5K. **H** Simulated cell morphologies for control and perturbed conditions, illustrating phenotypic differences predicted by the model. Colors indicate different time points in the simulation.

https://doi.org/10.1038/s41467-026-77894-2

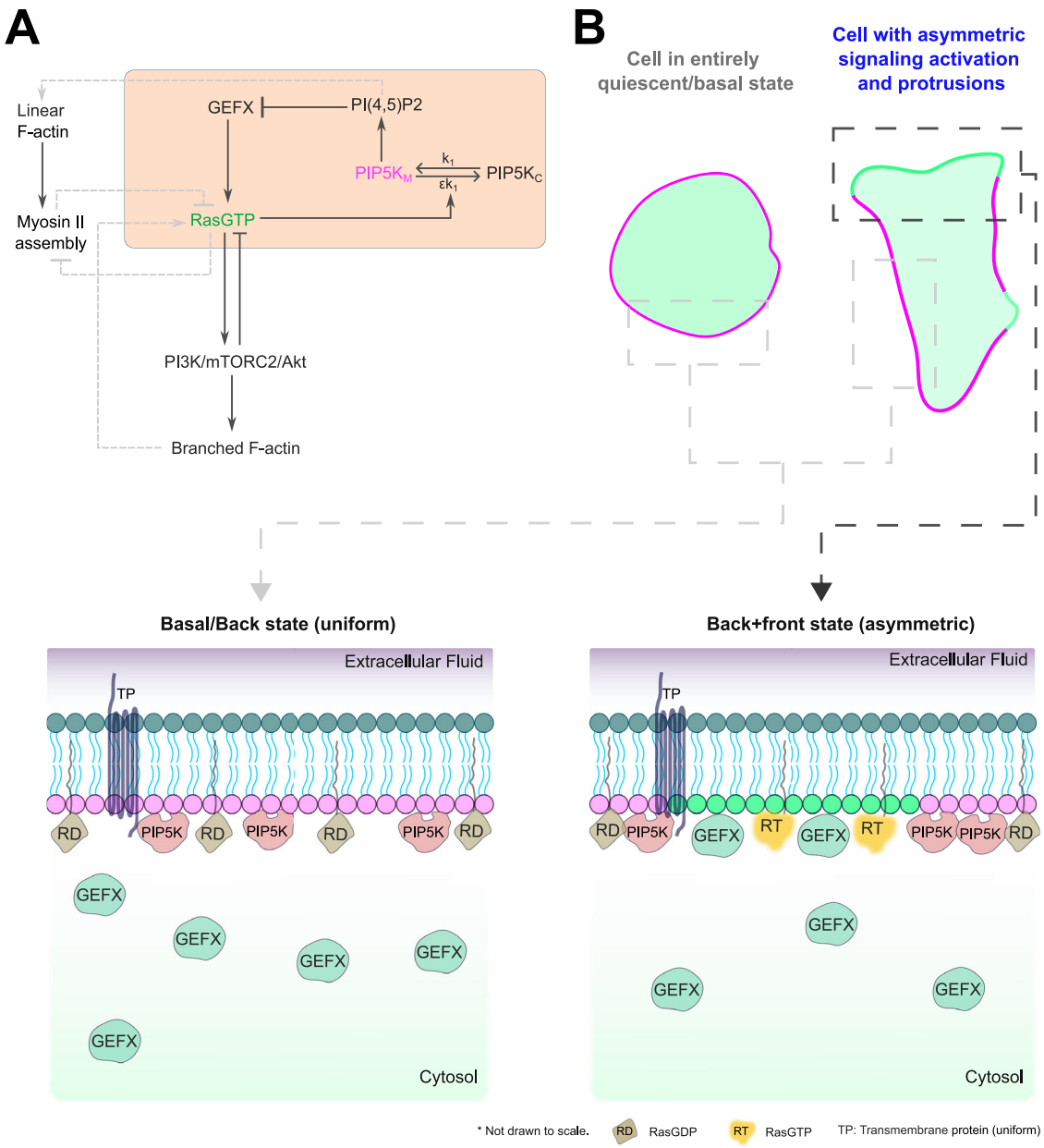


Fig. 8 | Schematic illustration showing the biophysical and biochemical bases of plasma membrane symmetry breaking. A Signal transduction network that regulate cell polarization and migration. Core signaling components that define the fundamental symmetry breaking and signal amplification are highlighted with a peach-colored box. M and C subscripts denote membrane and cytosol, respectively. Here, k1 is the membrane binding rate of PIP5K, ε is a small number that can be increased by RasGTP activity. Gray connections indicates positive and negative interactions with cytoskeletal components that are not essential for the symmetry breaking of the signaling network. **B** As a cell transitions from a back or inactivated(RasGDP) to a front or activated state (RasGTP), PIP5K molecules leave the front-state regions and associate back-state regions of the membrane. RasGDP is converted into RasGTP on the membrane via the action of recruited RasGEFX. The head groups of the inner leafletanionic lipids(PI(4,5)P2, PI(3,4)P2, PS, PA), enriched in the back stateregion, are shown in magenta. The head groups of other front lipid molecules are shown in green. Indicated transmembrane protein does not localize preferentially.

cortex is mostly actomyosin. Due to local stochastic fluctuations, some RasGEFX molecules approach the membrane, or some PIP5K molecules spontaneously dissociate from it. Ras activation leads to further PIP5K dissociation, lowering PI(4,5)P2 and amplifying a positive feedback loop. Meanwhile, more RasGEFX molecules are recruited to the membrane, thereby increasing Ras activation. Actomyosin is replaced by branched actin in this region.

Several elegant models for directional sensing and cell polarity have been proposed, but few explain the basic mechanisms underlying spontaneous symmetry breaking. Models that envision a local excitor and a more global inhibitor, generally referred to as LEGI models, allow local responses while blocking responses elsewhere[32,33,94]. In one version, the levels of the regulators are tied to receptor occupancy[34,94]. Other recent examples employ membrane tension[37,38] or cortical tension[95], which, as protrusions form, increases rapidly and globally, preventing protrusions elsewhere or membrane-cortical detachment, which specifically releases global inhibition at the front of the cell[41,42,96]. Other models involve membrane curvature, in which the recruitment of F-BAR-domain-containing proteins has been proposed to explain wave propagation[45]. Since all these systems require specific external cues or cytoskeletal activity, they cannot explain the initial symmetry breaking steps, which, in our model, intrinsically stem from differential localizations and mutual inhibitions between activated RasGEF/Ras and PIP5K/PI(4,5)P2.

The concept of mutual inhibition has been theorized from a systems perspective and tested in synthetic or in vitro systems in the past[97,98], but only a few models have focused on endogenous systems in living cells. These include mutual interaction between branched actin and linear actin/actomyosin[99], Rac1 and RhoA[100,101], and PI3K and PTEN[15,59]. These models are not inconsistent with the Ras-PIP5K model presented here. However, most of these models again rely on cytoskeletal activity and membrane deformation. The PI3K-PTEN scheme is independent of cytoskeletal activity, but perturbations produce less penetrant phenotypes: overproduction of PIP3 in *pten-* cells inhibits signaling and promotes actin polymerization, but the loss of PIP3 has only transient effects on migration[102,103]. In contrast, increases or decreases of Ras or PIP5K strongly alter multiple signaling pathways in different physiological scenarios such as propagating cortical waves, extended protrusions, macropinocytosis, polarized migration, and chemotaxis, and in cells lacking dynamic cytoskeletons. Consequently, we propose that, while compensatory and augmenting molecular events participate, the mutually inhibitory Ras-PIP5K circuit described here represents the core mechanism driving initial symmetry breaking, subsequent polarity, and governing a plethora of downstream physiological processes.

Our study shows that PI(4,5)P2 serves as one of the strongest negative regulators of Ras activity identified to date. Although various regulatory pathways for PI(4,5)P2 synthesis and degradation have been reported, our findings, together with prior literature, underscore the overarching importance of PIP5K in setting PI(4,5)P2 levels. In principle, PIP5K and PI(4,5)P2 can attenuate Ras signaling either by recruiting RasGAPs or by competing with RasGEFs, thus inhibiting Ras activation. The spontaneous appearance of RasGEFs, primarily GEFX in *Dictyostelium*, on protrusions and the requirement of GEFX for the hyperactivation of Ras induced by reducing PI(4,5)P2 suggest that high PI(4,5)P2 may inhibit Ras by preventing the access of GEFs to Ras. Some of the key questions for future research include: How are GEFs regulated by PI(4,5)P2? Are RasGAPs also regulated by PI(4,5)P2? How does activated Ras increase the dissociation of PIP5K from front regions? Are there other key feedback loops in this circuit, besides PIP5K, that could inhibit the network and balance elevated Ras activity[27]?

PI(4,5)P2 has been broadly implicated in cell migration and cancer signaling, acting not only as the precursor for IP3 and PIP3 but also as a modulator of numerous actin-binding proteins. In contrast to our results, several studies report that PI(4,5)P2 levels rise at the front and that some actin-binding proteins are activated by PI(4,5)P2[101,104,105]. Other actin-binding proteins are negatively regulated by PI(4,5)P2, and, consistent with our findings, some reports show PI(4,5)P2 localizing to the cell back[46,63,101]. Because the in vitro studies support both activating and inhibitory roles, the effects of PI(4,5)P2 on the actin cytoskeleton in living cells are difficult to predict a priori[106–117]. Our data, however, provide clear evidence that PIP5K and PI(4,5)P2 act as negative regulators in multiple physiological contexts across diverse cells and organisms.

These observations have significant implications for understanding disease and developing therapeutic strategies. On the surface, one might predict that PIP5K acts as an oncogene, given that PI(4,5)P2 is a substrate for PI3K and PLC, which promote oncogenic signaling axes, such as Akt and PKC pathways[118–123]. However, overexpression of PIP5K robustly suppresses Ras and PI3K activity across diverse systems, and reduction of PI(4,5)P2 clearly elevates PIP3 and hyperactivates Ras in the systems tested[47,124]. Thus, our results suggest that PIP5K should act as a tumor suppressor and the fact that it has not been reported as such may be due to redundancy of human subtypes. Nevertheless, strategies of increasing PIP5K or inhibiting it in cancer cells should be carefully considered and are likely to lead to effective therapeutic approaches.

Methods

Preparation of reagents and inhibitors

A 5 mM stock solution of Rapamycin (Sigma-Aldrich, 553210) was prepared by dissolving it in DMSO (Sigma-Aldrich, D2650). Latrunculin A (Enzo Life Sciences; BML-T119-0100) or latrunculin B (Millipore Sigma, 428020) was dissolved in DMSO to prepare the stock solutions of 5 mM. Jasplakinolide (Sigma-Aldrich, 420127) was purchased as a 1 mM stock solution. Folic acid (Sigma-Aldrich, 329823065) was first suspended in water, and then 2 M NaOH was added to prepare a 1.25 mM stock solution. Caffeine (Sigma-Aldrich,1085003) was dissolved in water to make 1 M stock solution. Fibronectin (Sigma-Aldrich, F4759-2MG) was initially dissolved in 2 mL water, and then further diluted in 8 mL $Ca^{2}+/Mg^{2+}$ free PBS to prepare the 200 μg ml^{-1} stock solution. N-Formyl-Met-Leu-Phe (fMLP; Sigma-Aldrich, 47729) was dissolved in DMSO to prepare the 50 mM stock solution. Phorbol 12-myristate 13-acetate (PMA; Sigma-Aldrich, P8139) was suspended in DMSO to make a 1 mM stock solution. FKP-(D-Cha)-Cha-r (Anaspec; 65121) was dissolved in PBS to prepare a 2.5 mM stock. A stock solution of EGF (Sigma-Aldrich, E9644) was generated by dissolving it in 10 mM acetic acid to a final concentration of 1 mg ml^{-1}. The anti-BSA mouse monoclonal antibody was acquired from Sigma-Aldrich (SAB4200688, clone BSA-33). Blebbistatin was dissolved in DMSO to prepare the 50 mM stock solution. ROCK inhibitor Y-27632 (Sigma-Aldrich, 688001) was dissolved in DMSO to prepare the 5 mM stock solution. Hygromycin B (Thermo Fisher Scientific, 10687010) and G418 sulfate (Thermo Fisher Scientific, 10131035) were acquired as 50 mg ml^{-1} stock solution. Blasticidin S (Sigma-Aldrich, 15205) or puromycin (Sigma-Aldrich, P8833) was dissolved in water to make the stock solutions of 10 mg ml^{-1} or 2.5 mg ml^{-1}, respectively. Doxycycline hyclate (Sigma-Aldrich, D9891-1G) was suspended in water to prepare the stock solution of 5 mg ml^{-1}. TRITC-dextran or FITC-dextran (Sigma-Aldrich, T1162) was dissolved in sterile water to prepare the 50 mg ml^{-1} stock solution. All stock solutions were aliquoted and stored at −20 °C unless otherwise mentioned.

Cell culture

Wild type *Dictyostelium discoideum* cells of the AX2 strain (dictyBase strain id DBS0235521) were obtained from the R. R. Kay laboratory (MRC Laboratory of Molecular Biology, UK) and cultured in HL5 medium at 22 °C. All *Dictyostelium* cells were used for experiments within maximum of 2 months after thawing from frozen stock. The *pikI-* cells (dictyBase strain ID DBS0350270), which was originally generated by Fets et al. (Strain ID HM1513)[69], were purchased from dictyBase/Dicty Stock Center[125,126]. *pikI–* cells were grown on a *Klebsiella aerogenes* lawn on an SM plate and transferred to HL5 medium supplemented with heat-killed *Klebsiella aerogenes* before the experiment. *gefX-, gefB-, gefU-, and gefM-* cells were generated at the Ueda lab, as described previously[27]. *Gβ-* cells were generated in the Devreotes Lab previously[85]. *abnABC-* cells were also generated previously in the Devreotes Lab[127]. GFP-arpC cells were purchased from Dictybase (strain ID DBS2036065). Growth phase cells were used as starting point in all the *Dictyostelium* experiments, unless otherwise mentioned.

The human HL-60 cell line was obtained from the O. D. Weiner laboratory (UCSF) and cultured in RPMI 1640 medium (Gibco, 22400-089) with 15% heat-inactivated fetal bovine serum (Thermo Fisher, 16140071). To obtain differentiated neutrophil-like cells, HL-60 culture media was supplemented with 1.3% DMSO and ~1.5 million cells were maintained in that media for 5–7 days[128]. To obtain differentiated macrophage-like cells, HL-60 culture media was supplemented with 32 nM PMA for 2-3 days[129].

RAW 264.7 murine macrophage-like cells were obtained from the N. Gautam laboratory (Washington University School of Medicine in St. Louis) who originally acquired these cells from the Washington University Tissue Culture Support Center and American Type Culture Collection (ATCC, TIB-71). These cells were maintained in Dulbecco's

modified Eagle's medium (DMEM) containing 4500 mg l^{-1} glucose, l-glutamine, sodium pyruvate, and sodium bicarbonate (Sigma-Aldrich, D6429), supplemented with 10% heat-inactivated fetal bovine serum (ThermoFisher Scientific, 16140071) and 1% penicillin–streptomycin (ThermoFisher Scientific, 15140122). When 70–90% confluency was reached, RAW 264.7 cells were gently lifted using cell scrapers (SARSTEDT, 83.1830) and subcultured using 1:5-1:10 split ratio.

MDA-MB-231 breast cancer cell lines were obtained from M Iijima laboratory (School of Medicine, Johns Hopkins University). These cells were cultured in DMEM medium with high glucose and GultaMAX™ (ThermoFisher Scientific, 10566024), supplemented with 10% heat-inactivated fetal bovine serum (ThermoFisher Scientific, 16140071) and 1% penicillin–streptomycin (ThermoFisher Scientific, 15140122). When 70–90% confluency was reached, MDA-MB-231 cells were detached using 0.05% Trypsin-EDTA (ThermoFisher Scientific, 25300054) and subcultured using 1:5–1:10 split ratio.

All mammalian cells were grown in humidified conditions at 5% CO2 and 37 °C. All the experiments were conducted using low passage number cells.

DNA constructs

All DNA oligonucleotides were purchased from Sigma-Aldrich. *Dictyostelium* PIP5K was PCR amplified from genomic DNA and cloned into the pCV5-GFP expression plasmid to generate PIP5K-GFP (pCV5). Two-point mutations K681N and K682N were introduced to PIP5K-GFP (pCV5) to generate PIP5K (K681N, K682N)-GFP (pCV5). PIP5K was then PCR amplified and cloned into doxycycline-inducible pDM335 plasmid (dictyBase, ID no. 523) using BglII/SpeI restriction digestion to generate mRFPmars-PIP5K (pDM335). mRFPmars-PIP5K was than PCR amplified and cloned into doxycycline-inducible pDM359 plasmid (dictyBase, ID no. 518) using BglII/SpeI restriction digestion to generate mRFPmars-PIP5K (pDM359). mRFPmars was then replaced with EGFP to generate EGFP-PIP5K (pDM359). EGFP was then replaced with KikGR to generate KikGR-PIP5K (pDM359). KikGR was then replaced with Halo to generate Halo-PIP5K (pDM359). DNA sequences encoding the 301–718aa amino acids of PIP5K, were PCR-amplified from PIP5K-GFP (pCV5) and cloned into pCV5-GFP vector. DNA sequences encoding the 1–315aa amino acids of PIP5K, were PCR-amplified from PIP5K-GFP (pCV5) and cloned into mCherry-FRB-MCS (pCV5) expression plasmid (previously created in the Devreotes Lab) using NheI/XhoI restriction digestion to generate mCherry–FRB-PIP5K (1-315aa) (pCV5). DNA sequences encoding the 316–718aa amino acids of PIP5K, were PCR amplified and cloned into mRFPmars-SspBR73Q-MCS (pCV5) using NheI/NotI restriction digestion to generate mRFPmars-SspBR73Q-PIP5K (316–718aa). DNA sequences encoding the 301-718aa amino acids of PIP5K, were PCR amplified and cloned into pCV5-GFP expression plasmid to generate PIP5K (301–718aa)-GFP (pCV5). PH-PLCδ-YFP (pCV5), CynA-KikGR (KF2), RBD-EGFP (pDM358), PHcrac-RFP (pDRH), LimEΔcoil-mCherry (pDM181), PHcrac-YFP (pDM358), LimEΔcoil-RFP (pDRH), cAR1-FKBP-FKBP (pDM358 or pCV5), mCherry-FRB-MHCKC (pCV5), and $PKBR1_{N150}$-iLiD (pDM358) were previously created in the Devreotes Lab. Myosin II-GFP (pDM181) was obtained from the D. Robinson laboratory (School of Medicine, JHU). Rat PAK1(GBD)-YFP (pDEXH) was a gift from the C. Huang lab (School of Medicine, JHU). RBD-RFP (pDM358) was purchased from dictyBase (ID no. 472).

For transient transfection in RAW 264.7 macrophage-like cells and MDA-MB-231 cells, PH_{Akt}-mCherry and CIBN-CAAX (Addgene #79574) were obtained from Devreotes Lab stock. EGFP-PIP5K1B (Addgene #202722), GFP-PIP5K1γ90 (Addgene #22299) TagBFP-FKBP-PIP5K1C (Addgene #220090) (cytosolic PIP5K1C), and mCherry-NES-SspB-MCS-iLiD-CAAX (Addgene #173869) were purchased from Addgene. The mCherry was replaced with Crimson fluorescent protein, and a point mutation R73Q was introduced to SspB to generate Crimson-NES-SspBR73Q-MCS-P2A-iLiD-CAAX (previously generated in Devreotes Lab). Cytosolic, functional PIP5K1C was obtained from G. R. V. Hammond lab (University of Pittsburgh School of Medicine) and then PCR amplified and cloned into the XhoI/EcoRI sites of the Crimson-NES-SspBR73Q-MCS-P2A-iLiD-CAAX expression plasmid to generate Crimson-NES-SspBR73Q-PIP5K1C-P2A-iLiD-CAAX (Opto-RecP). Venus-iLiD-Mito (Addgene #60413) was purchased from Addgene. iLiD-CAAX was replaced with iLiD-Mito to generate Crimson-NES-SspBR73Q-MCS-P2A-iLiD-Mito. MCS was replaced with full-length PIP5K1B to generate Crimson-NES-SSPBR73Q-PIP5K1B-P2A-iLiD-Mito (Opto-SeqP).

For stable lines in HL-60 cells, cells co-expressing LifeAct–miRFP703 (pLJM1) (Addgene #201750) and CIBN-CAAX (pLJM1) (Addgene #201749) or RFP-PHAkt (pFUW2) were previously created in the Devreotes Lab[124]. EGFP-PIP5K1B and EGFP-PIP5K1C were PCR amplified and cloned into the BspEI/SalI sites of the PiggyBac transposon plasmid to generate EGFP-PIP5K1B (pPB) and EGFP-PIP5K1C (pPB). For stable lines in MDA-MB-231 cells, stable lines expressing GFP-PIP5K1C (pPB-TRE, Addgene #104454) were made under a doxycycline-inducible promoter.

Transfections, nucleofections, and lentiviral transduction

The *Dictyostelium* cells were transfected using a standard electroporation protocol[25,26]. Briefly, for each transfection, 5×10^6 growth phase cells were collected and then washed 2X with ice-cold H-50 buffer (20 mM HEPES, 50 mM KCl, 10 mM NaCl, 1 mM MgSO4, 5 mM NaHCO3, 1 mM NaH2PO4, pH adjusted to 7.0), and finally resuspended in 100 µl ice-cold H-50 buffer. Around 2 µg of total DNA was added to this cell suspension for each transfection and then the entire mix was quickly transferred to an ice-cold 0.1-cm-gap cuvette (Bio-Rad, 1652089) for two rounds of electroporation at 850 V and 25 µF in Bio-Rad Gene Pulser Xcell Electroporation Systems, maintaining 5 s interval between the pulses. After electroporation, cuvettes with cells were incubated on ice for 10 min and then the the cells were transferred to a 10-cm Petri dish containing HL-5 medium. The cells were selected by the addition of hygromycin B (50 µg ml^{-1}) and/or G418 (20–30 µg ml^{-1}) after 24 h according to the correct antibiotic resistance of the vectors.

RAW 264.7 cells and MDA-MB-231 cells were nucleofected in an Amaxa Nucleofector II device using Amaxa Cell line kit V (Lonza, VCA-1003) by slightly modifying pre-existing protocols[26,130]. For every nucleofection, 3×10^6 cells were harvested, washed, and resuspended in 100 µl of supplemented Nucleofector Solution V. A total of 2–3 µg of plasmid DNA mixture was combined with the cell suspension and quickly transferred to a Lonza cuvette for electroporation using the program settings D-032 and X-013, for RAW 264.7 cells and MDA-MB-231 cells, respectively. Immediately, pre-warmed and pH-adjusted culture medium (500 µl) was added to the electroporated cells in the cuvette. The cell suspension was then carefully transferred to a 1.5 ml vial and incubated at 37 °C and 5% CO2 for 10 min and 30 min for RAW 264.7 cells and MDA-MB-231 cells, respectively. Next, 50–100 µl solution containing cells was transferred to a 8-well Nunc coverslip chamber and incubated for around 1 h so that cells can adhere to the coverslips. Finally, approximately 400 µl of pre-warmed, pH-adjusted culture medium was added to each chamber. RAW 264.7 cells were further incubated for 4–6 h before imaging. MDA-MB-231 cells were incubated overnight and imaged the next day.

Stable lines involving HL-60 cells or MDA-MB-231 cells were engineered by using 2nd or 3rd generation lentiviral systems and/or PiggyBac transposon-integration based methods[124,131]. Stable transposon-based integration in the HL-60 and MDA-MB-231 lines was achieved by electroporating 2×10^6 cells with 5 µg of the transposon plasmid together with an equal quantity of the transposase expression plasmid, using the Neon™ transfection kit (Invitrogen, MPK10025B). Cells and DNA were combined in buffer "R" and pulsed at 1350 V for 35 ms in 100 µl Neon™ tips on a Neon™ electroporation system (Invitrogen, MPK5000). Electroporated cells were seeded into 6-well plates in mixed culture medium and left to recover for 24 h before selection

began. Selection proceeded for 5–6 days in either blasticidin S (10 μg /mL) or puromycin (2.5 μg/mL). Following withdrawal of blasticidin S, the surviving population was transferred to 48-well plates (Sarstedt, 83.3923) and expanded over 2-4 weeks to establish stable lines, with selection antibiotic retained in the medium thereafter.

For lentivirus transfection, 2nd or 3rd generation virus was generated in HEK293T cells. Usually, lentiviral particles were produced by co-transfecting HEK293T cells with 2 μg pMD2.G (Addgene #12259), 8 μg psPAX2 (Addgene #12260) and 10 μg of the relevant transfer plasmid per reaction, delivered using Lipofectamine 3000 according to the supplier's protocol (Invitrogen, L3000-008). Ninety-six hours later the virus-bearing supernatant was collected and cleared of debris by centrifugation (3000 rpm, 20 min, 4 °C). HL-60 cells, plated into multiple wells of 6-well plates (Greiner Bio-One, 657160) at 0.25×10^6 cells/mL to a total of 4×10^6 cells, then received the entire volume of cleared supernatant together with polybrene at 10 μg/mL. The inoculum was withdrawn after 24 h and replaced with a blend of fresh and conditioned medium. Five days post-transduction the population was expanded to 80% confluency and sorted to enrich for high expressors: cells were pelleted, taken up in sorting buffer (Ca^{2+}/Mg^{2+}-free 1× PBS containing 0.9% heat-inactivated FBS and 2% penicillin-streptomycin) at 15×10^6 cells/mL, and passed through a 100 μm microfluidic sorting chip. The brightest ~5% were harvested into fresh medium supplemented with 2% penicillin-streptomycin and grown to ~90% confluency before expansion.

Retroviral production for primary T cell transduction

To produce retroviral particles for overexpression of PIP5K1C, 293 T cells (originally obtained from ATCC) were grown to 70% confluency in 6-well plates before being co-transfected with 4.5 μg mNeon-PIP5K1C (or mNeon alone as a control, in the MSCV backbone, VectorBuilder) along with 3.5 μg pCL- eco packaging vector (Addgene #12371). Transfection was done using calcium phosphate purchased from Invitrogen (cat# K278001). Transfection mixes remained on 293 T cells overnight before being replaced with fresh media, after which cells were incubated for an additional 24–30 h. Retroviral containing supernatants were collected and centrifuged for 10 min at $1000 \times g$ to remove cellular debris, and polybrene was added at a final concentration of 8 μg/mL. Retroviral supernatants were then immediately applied to T cells for transductions.

To generate lifeact-mScarlet retroviral particles, 4.5 μg lifeact-mScarlet (MSCV backbone, VectorBuilder) and 3.5 μg pCL- eco packaging vector were co-transfected into 293 T cells and harvested as above.

Primary CD8+T cell isolation and transduction

Primary CD8 + T cells were isolated from spleen and lymph nodes of WT B6 mice (C57BL/6J, strain #000664, 8–12 weeks old). Mice were purchased from The Jackson Laboratory and housed at Upstate Medical University mouse facility in accordance with the Institutional Animal Care and Use Committee guidelines. Briefly, spleens and lymph nodes were homogenized and filtered before incubation with ACK lysis buffer (77 mM NH_4Cl, 5 mM $KHCO_3$, and 55 μM EDTA pH 7.2–7.4) for 1 min to remove red blood cells (RBC). After RBC lysis, cells were washed and incubated with anti-$CD4^+$ (clone GK1.5) and anti-MHCII (clone M5/114) for 20 min at 4 °C. Followed by magnetic separation using BioMag Goat anti-rat IgG beads (Qiagen cat#310107). Isolated $CD8^+$ T cells were then immediately activated on a 24-well plate coated with 5 μg/mL anti-CD3 (clone 2C-11) and 2 μg/mL anti-CD28 (clone PV-1) at 1×10^6 cells per well. Activation was done in T cell media composed of Corning DMEM supplemented with 5% FBS, 1% each penicillin/streptomycin, non-essential amino acids, and Glutamax (all purchased from Gibco), plus 2 μL 2-mercaptoethanol (obtained from Sigma Aldrich). Twenty four hours later, the T cell media was collected and put aside for cell culture post-transduction. Eight hundred microliters of viral supernatants were gently added per well and plates were incubated at 37 °C for 10 min. Plates were centrifuged at $1100 \times g$ for 2 h at 32 °C. Plates were then incubated at 37 °C for 10 min and then viral supernatants were removed and replaced with 1.5 mL of pre-collected conditioned media mixed with fresh complete T cell medium at a 2:1 volume ratio. T cells were cultured for an additional 24 h before being removed from activation and mixed at a 1:1 volume ratio with fresh T cell media containing recombinant 80 U/mL IL-2 to create a final concentration of 40 U/mL. T cells were used on days 5–6 post-harvest for all experiments.

To generate lifeact-mScarlet expressing T cells, $CD8^+$ T cells were transduced as above with 200 μL of lifeact-mScarlet viral supernatants along with 600 μL of mNeon-PIP5K1C or mNeon alone.

CRISPR/Cas9 to generate *gefX-/pikI-* cell line

We slightly modified a pre-existing protocol for using CRISPR/Cas9 system to target specific genes and generate KO mutants in *Dictyostelium* cells[132]. gRNA guide sequences targeting gefX gene were designed using Cas-Designer (http://www.rgenome.net/cas-designer/). Custom gRNA oligos were purchased from Sigma-Aldrich. This selected gRNA sequence TCAAACTTTGGTCTAGTTAA (forward) was then cloned into pTM1285 plasmid that was obtained from the D Robinson laboratory (School of Medicine, JHU). The *pikI-* cells were transfected with pTM1285 plasmid containing gefX gRNA using standard electroporation (as described above). After 8–16 h of electroporation, the existing media was replaced with HL-5 media containing G418 (20–30 μg ml^{-1}). Cells were cultured for 3 more days in that media. Next, floating cells were washed off and remaining live cells were plated on SM plates with cultured *Klebsiella aerogenes* and incubated at room temperature for 3–4 d until isolated plaques formed. These plaques were then individually transferred to 96-well plates containing HL-5 medium without any G418. As cells grew for 2–3 days, genomic DNA was extracted for PCR verification and the clones were subsequently transferred to 6-well plate and finally to 10-cm Petri dishes and grown to ~90% confluency.

Microscopy

All *Dictyostelium* experiments were performed on a 22 °C stage. All RAW 264.7, MDA-MB-231, and HL-60 experiments were performed inside a 37 °C heated chamber with 5% CO_2 supply. Majority of the time-lapse live-cell imaging experiments were performed using one of the following microscopes: (1) Zeiss LSM 780-FCS Single-point, laser scanning confocal microscope (Zeiss Axio Observer with 780-Quasar; 34-channel spectral, high-sensitivity gallium arsenide phosphide detectors), (2) Zeiss LSM800 GaAsP Single-point, laser scanning confocal microscope with wide-field camera, (3) Nikon Eclipse Ti-E dSTROM total internal reflection fluorescence (TIRF) microscope (Photometrics Evolve EMCCD camera). The Zeiss 780 confocal microscope was regulated using ZEN Black software; Zeiss 800 confocal microscope was operated using ZEN Blue software; the Nikon TIRF was driven by Nikon NIS-Element software. The 40X/1.30 or 63X/1.4 Plan-Neofluar oil objective (with appropriate digital zoom) was used in all microscopes. The 488 nm (Ar laser) excitation was used for GFP and YFP, 561 nm (solid-state) excitation was used for RFP and mCherry, and 633 nm (diode laser) excitation was used for miRFP703 in Zeiss 780 and 800 confocal microscopes. The 488 nm (Ar laser) excitation was used for GFP and 561 nm (0.5 W fiber laser) excitation was used for mCherry and RFP in Nikon TIRF.

Cell preparation for live-cell imaging

Before starting the image acquisition, growth phase vegetative *Dictyostelium* cells (unless otherwise mentioned) were put on an eight-well coverslip chamber (Nunc Lab-Tek), allowed to adhere for ~15–20 min, and then HL-5 media was aspirated and replaced with 400–500 μL DB media (Development buffer: 5 mM Na2HPO4 and 5 mM KH2PO4 supplemented with 2 mM MgSO4 and 0.2 mM CaCl2). Cells were incubated in DB for ~40–60 min before starting imaging

experiments. For details on the preparation of developed or electrofused *Dictyostelium* cells for imaging, please see *"Cell differentiation"* and "Electrofusion" sections below.

Differentiated HL-60 macrophages were allowed to adhere on similar surface for ~40 min. Differentiated HL-60 neutrophils, pretreated with heat-killed *Klebsiella aerogenes*, were allowed to adhere on fibronectin-coated 8-well chambers for ~20 min. Next, for either HL-60 neutrophils or macrophages, the culture media was gently switched with fresh RPMI 1640 medium and the adhered cells in fresh media were used for imaging. MDA-MB-231 cells were introduced to 8-well chamber the ~12 h before the experiment, as described in the "Transfections, nucleofections, and lentiviral transduction" section. Spent culture media was exchanged with fresh culture media right before the experiments. For more details on wound healing and 3D spheroid assays with MDA-MB-231 cells, please see the relevant sections below. Generally, after nucleofection and adhesion to the substrate (see above), RAW 264.7 cells were imaged in warm, pH adjusted Hank's balanced salt solution (HBSS buffer) supplemented with 1 g/L glucose. For more details on RAW 264.7 cell preparation for microscopy, please see relevant sections below.

To induce PIP5K expression, doxycycline (50 μg ml^{-1} for Dictyostelium cells, 1 μg ml^{-1} for MDA-MB-231 cells) was added 12 h before imaging. For macropinocytosis assay, *Dictyostelium* cells were incubated with 2 mg/ml TRITC-dextran or FITC-dextran for 10 min, washed twice with DB and imaged afterwards. For recording protrusion or macropinosome dynamics, confocal imaging was performed at a middle z-plane of the cells. Images were acquired at a frequency of 5 s-2 min per frame, as appropriate. To visualize cortical/ventral waves in *Dictyostelium* and HL-60 macrophage cells, either confocal microscopes were focused on the very bottom of the cell to capture the substrate-attached ventral surface of the cell, or TIRF microscopy was used.

For the cytoskeletal dynamics inhibition experiments, neutrophils were treated with 10 μM Y-27632 for at least 10 min before imaging and 8 μM jasplakinolide and 5 μM latrunculin B were added during imaging, as described elsewhere[89]. In *Dictyostelium*, for myosin II or branched actin inhibition experiments, 50 μM blebbistatin or 100 μM CK666 was added during imaging, respectively. For arresting actin polymerization in *Dictyostelium* cells, 5 μM latrunculin A and 4 mM caffeine were added at least 20 min before imaging (note that, caffeine induce increased wave propagation in cells, as reported previously[14,15,26]).

To image primary CD8 + T cells, Ibidi 8-well, glass-bottomed chamber slides were coated with ICAM-1 at 2 μg/mL (Bio-Techne) overnight at 4 °C. Activated, transduced $CD8^+$ T cells were washed and resuspended in Leibovitz's L-15 medium (Gibco) containing 2 mg/mL D-glucose and 5×10^4 cells were added to each well. After 20 min, wells were gently washed to remove non-adherent cells and debris and mounted on a Marianas system (3i) consisting of a Ziess Axio Observer 7 equipped with a X-Cite mini+ light source (Excelitas) and a Prime BSI Express CMOS camera (Photometrics) enclosed in an environmental chamber (Okolab). For cell tracking, movies were collected every 30 s for 10 min using a 20× objective at 37 °C with SlideBook software (3i) and exported to ImageJ for analysis. mNeon expressing cells were tracked using the manual tracking plugin to generate XY coordinates for each time point. We only included cells that stayed in the field-of-view for the entire imaging period. 20× movies were also obtained with higher time resolution (2 s per timepoint). 63× imaging was performed every 3 s for 1 min total.

Electrofusion

Dictyostelium cells were elecrofused to form giant cells using an established protocol[9,25]. First, the growth phase cells were collected from suspension culture, washed twice, and finally resuspended in 10 ml SB buffer (17 mM Soerensen buffer containing 15 mM KH_2PO_4 and 2 mM Na_2HPO_4, pH adjusted to 6.0) at a density of 1.5×10^7 cells/mL. Next, to facilitate the formation of large cell clusters, the cells were placed in a 50 mL conical tube and gently rolled for 30 to 40 min. Following this, 800 μL of the rolled cells with visible large clusters were moved to a Bio-Rad cuvette with a 0.4 cm gap. This transfer was carried out using pipette tips with their edges cut off to ensure the cell clusters remained intact. To induce plasma membrane hemifusion, electroporation was conducted using a BioRad Gene Pulser (Model 1652098). The procedure involved one pulse at 1 kV and 3 μF, followed by two more pulses at 1 kV and 1 μF. A time interval of 3 s was maintained between each pulse. After electroporation, approximately 35 μL of the electrofused cells were extracted from the cuvette and placed into a Nunc Lab-Tek 8-well chamber. The cells were incubated for 5 min, after which 450 μL of SB buffer supplemented with 2 mM CaCl2 and 2 mM MgCl2 was added gently to the well. Finally, the cells were incubated for about 1 h to recover, settle, and adhere to the substrate before the image acquisition was initiated.

Frustrated phagocytosis and osmotic shock

To record the ventral wave dynamics in HL-60 macrophages that had been differentiated with PMA, we made minor adjustments to an existing protocol[26,62]. First, the Nunc Lab-Tek eight-well coverslip chambers were prepared. This involved an initial pre-wash with 30% nitric acid, followed by a 3-h coating with 1 mg ml^{-1} BSA. The chambers were then washed with PBS and incubated for 2 h with 5 μg ml^{-1} anti-BSA antibody (a 1:200 dilution). A final double wash with PBS was performed to remove any excess antibodies. Before imaging, the transfected and PMA-differentiated macrophage cells were starved for 30 min in a suspension of 1× Ringer's buffer. This buffer consisted of 150 mM NaCl, 5 mM KCl, 1 mM CaCl2, 1 mM MgCl2, 20 mM HEPES, and 2 g l^{-1} glucose, with a pH of 7.4. Finally, these starved cells were transferred to the prepared, opsonized chambers. The cells were allowed to spread on the antibody-coated surface for 5 to 10 min. Just before the imaging, a hypotonic shock was induced by applying a 0.5× Ringer's solution.

Optogenetics

Optogenetics perturbation experiments were performed in *Dictyostelium*, RAW 264.7, or MDA-MB-231 cells by slightly modifying established protocols[25,124,133]. To test the necessity and sufficiency of plasma membrane PIP5K in regulating symmetry breaking and protrusion formation, newly engineered Opto-SeqP was introduced in RAW 264.7 macrophages whereas Opto-RecP was introduced in RAW 264.7 macrophages as well as MDA-MB-231 cells, using nucleofection (please see *"DNA constructs"* and *"Transfections, nucleofections, and lentiviral transduction"* sections for more details). In parallel, Opto-CTRL system was also introduced in these cell lines as a control for optogenetic phenotypes. Note that, cytosolic, functional version of PIP5K1C had been recently reported[87] which we used to engineer Opto-RecP, as described above. In all cases, 561 nm excitation laser was used to track the localization dynamics of mCrimson-SspB or mCherry-SspB tagged recruitee and 488 nm excitation laser was used to trigger the optogenetic recruitment. The 633 nm excitation was used to record the Lifeact-miRFP703 dynamics throughout the experiment. Before turning 488 nm laser ON, the basal activities was recorded for 5–10 min, whereas after turning 488 nm laser ON, recruitment induced activities were recorded for another 30–40 min. For Opto-Rec system, the RAW 264.7 cells were globally stimulated with saturating dose of C5aR agonist immediately after tagged PIP5K was localized to plasma membrane by turning ON 488 nm laser; the MDA-MB-231 cells were maintained in saturating dose of EGF throughout the experiment. For Opto-SeqP recruitment, cells were not stimulated with any external agonist and maintained in standard HBSS media.

Chemically induced dimerization and targeted screening through RasGEFs

To identify which RasGEFX mediate lowered PI(4,5)P2-driven Ras activation, we screened across the *Dictyostelium* RasGEF space which has 25 members (RasGEFA to RasGEFY). First, we analyzed the data from Iwamoto et al.[27], where all RasGEFs were hierarchical clustered based on their ability to induce spontaneous Ras activity when overexpressed. We selected all four members of "Cluster 1" from there and decided to trigger acute PI(4,5)P2 lowering in cells where these RasGEFs are knocked out. To this end, RasGEFB, RasGEFM, RasGEFU, and RasGEFX were knocked out from wild-type AX2 Dictyostelium cells at the Ueda lab, as described previously[27] and following plasmids were stably expressed in the knockout and control wild-type cells: (a) cAR1-FKBP-FKBP (pDM358) as the membrane anchor and (b) mCherry-FRB-Inp54p (pCV5) as recruitable enzyme for rapidly hydrolyzing PI(4,5)P2. Note that, this Inp54p-based chemically inducible dimerization system is a well-established synthetic PI(4,5)P2 lowering tool[16,17,25,134]. Finally, on the day of imaging experiment, engineered *Dictyostelium* cells were transferred to an eight-well coverslip chamber and prepared as described in detail in previous section "*Cell preparation for live-cell imaging*". After imaging a certain number of frames, rapamycin was added gently to the chamber (to a final concentration of 5 µM) during image acquisition to facilitate the recruitment of Inp54p to the plasma membrane and imaging was continued. Cell migration speed (before and after recruitment) and percent of fans and oscillators were quantified using a custom-written Python-based workflow. Please see Image Analysis section and GitHub repo for further details.

To facilitate myosin II disassembly from the membrane-cortex in PIP5K overexpression cells, an analogs rapamycin inducible dimerization system was used that was previously developed at the Devreotes Lab by incorporating MHCKC as recruitee[81]. To generate data for Fig. S6D, mCherry–FRB-PIP5K$_{1\text{-}315aa}$ (pCV5) was used as recruitee. In both cases, cAR1-FKBP-FKBP (pDM358) was used as membrane anchor.

2D wound healing assay

The wound healing assay was performed using Ibidi Culture-Insert 4 Well in µ-dish 35 mm, high (Ibidi, catalog # 80466). Around 6×10^5 MDA-MB-231 cells expressing doxycycline-inducible PIP5K1C were seeded in each insert well and incubated for 24 h until a full monolayer was created. Next day, 1 µg/ml Dox was added to each monolayer to induce PIP5K1C expression. After another 16 h Dox incubation, the 4-well insert was removed, creating a 500 µm cell-free area between cell monolayers. Cells were imaged using Zesis 780 Confocal microscopy with 20× objective, 5 × 5 tile function. The open scratch area was quantified at 1 h, 15 h, and 24 h time points.

3D organoid assay

MDA-MB-231 cells expressing doxycycline-inducible PIP5K1C were trypsinized and resuspended at a concentration of 1×10^5/ml in normal culture media. Spheroids were formed by putting 20 µl of cells in form of hanging droplets onto the underside of a 10-cm petri dish for 72 h. At 72 h, 2 µg/ml Dox was added to each drop to induce PIP5K1C expression. Next day, spheroids were collected in a tube previously coated with 2.5% (vol/vol) BSA solution in DPBS. After centrifugation at 400 × *g* for 5 min, spheroids were resuspended in growth-factor-reduced Matrigel (Corning, 354230). Spheroids were embedded at a density of 1 spheroid per µl into the Matrigel solution and 50 µl of suspension per well was plated into an 8-well glass-bottomed chamber on a 37 °C heating block. Following a 1-h incubation at 37 °C, 0.5 ml of normal medium was added to each well. Spheroids were disseminated into Matrigel over a period of 8 h to 3 days. Spheroid images were acquired by a Zesis Confocal LSM 780 microscope with a 40× water objective. Dissemination of spheroids was quantified using Fiji/ImageJ by outlining the core of the spheroid and the total spheroid area (dissemination strand and core).

Cell differentiation

For *Dictyostelium* cell development, a well-established protocol was followed[25,135,136]. Briefly, 8×10^7 growth phase cells were harvested from suspension culture and pelleted. Next, the cells were washed twice with DB and then resuspended in 4 ml DB in a conical flask. Cell suspension in the conical flask was shaken at 105 r.p.m. for 1 h. The cells were then pulsed with 50–100 nM cAMP (5 s pulse every 6 min) using a time-controlled peristaltic pump for 5–6 h while shaking was continued. This allowed the cells to correctly develop and polarize. After development, around 10–15 µL of differentiated cells were picked up from the shaking conical flask and put onto an eight-well coverslip chamber. Cells were then resuspended in 450 µl DB and incubated for ~30 min before imaging.

For development on non-nutrient agar, an existing protocol[137] was followed with slight modifications. The growth phase cells were collected, washed twice with DB buffer, and resuspended in DB with a density of 5×10^6 cells/mL. Around 1 mL of such cell suspension was added to a well of a 6-well plate which contained pre-solidified DB agar. The development process was visualized in stereoscopes for next 24 h.

Global receptor activation assay

For cAMP receptor (cAR1) activation experiments, *Dictyostelium* cells were first differentiated in suspension as described in "Cell differentiation" section. Cells were treated with 5 µM Latrunculin A (final concentration) for around 20 min before imaging. Using Zeiss LSM 780 microscope, 10–20 frames were first recorded to identify the basal activity of the proteins before receptor activation, then cAMP was gently added to the 8-well chamber (to a final concentration of 1 µM) as that can robustly activate cAR1. The image acquisition was continued throughout where one frame was recorded after each 3 s.

For folate receptor (fAR1) activation experiments, vegetative growth phase *Dictyostelium* cells, cells were seeded on the eight-well coverslip chamber and incubated for 20–30 min. Then, the HL5 medium was replaced with DB and incubated cells with an additional 20 min before the imaging (as described in detail above). As in cAR1 activation, cells were then treated with 5 µM Latrunculin A (final concentration) for around 20 min. Using Zeiss LSM 780 microscope, 10–20 frames were first recorded to identify the basal activity of the proteins, then folic acid was added to the chamber (to a final concentration of 0.1, 1, 10, or 100 nM) to activate the fAR1 receptors, and the image acquisition was continued. Similar to cAR1 activation, an imaging frequency of 3 s/frame was maintained during the experiment.

For C5aR global activation in RAW 264.7 cells, a pre-existing protocol was followed[26]. Briefly, RAW 264.7 cells expressing either PH_{Akt}-mCherry only or co-expressing PIP5K-GFP and PH_{Akt}-mCherry, were collected after 4–6 h of nucleofection (as described in "*Transfections, nucleofections, and lentiviral transduction*" section). The culture medium was then replaced with HBSS buffer supplemented with 1 g/L glucose and cells were incubated for another 30 min before the imaging. Using a confocal laser scanning microscope, 10–20 frames were first acquired to record the basal activity of the proteins before stimulation, then C5aR agonist FKP-(D-Cha)-Cha-r was added to the chamber wells (to a final concentration of 0.1, 1, 10, or 100 µM) to activate the C5a receptors, and the image acquisition was continued. An imaging frequency of 15 s/frame was maintained throughout the experiment.

2D Chemotaxis Assay

We slightly modified a pre-existing protocol to perform chemotaxis assay for *Dictyostelium* cells[26,138]. Briefly, vegetative cells were seeded on the 1-well Nunc Lab-Tek chamber as a drop at the center and

incubated for 20–30 min. Then 2 mL DB buffer was added to the chamber and cells were distributed by thoroughly pipetting a few times. Next, 10 µM of folic acid solution was filled in a Femtotip microinjection needle and then the needle was connected to a FemtoJet microinjector (Eppendorf). The microinjector emitted folate in a continuous injection mode where a compensation pressure of 15 hPa was maintained throughout generally. To trigger the chemotaxis process in a particular field of view, a programmed micromanipulator was used to bring the micropipette to the (x,y,z) coordinate of that particular field of view. The imaging was performed with an acquisition frequency of 30 s/frame.

Multinucleation assay

Dictyostelium cells that have been in suspension at 200 rpm for 2–3 days, or cultured on adherent surface, were seeded at ~70% confluency on glass coverslips in HL-5 medium. After cells were allowed to adhere to the coverslip for 20 min, the HL-5 medium was exchanged with ice-cold fixative solution (2% PFA + 0.01% Triton X-100 in 1.5× HL-5 medium) and incubated for 10 min. Cells were then washed quickly with 1x PBS, and the nuclei were stained with 10 µg/ml Hoechst for 10 min. Afterwards, cells were washed three times, 10 min each time, with 1× PBT (1× PBS + 0.01% Triton X-100). Before microscopy, cells were mounted on coverslips using Invitrogen SlowFade™ Gold antifade reagent. Cells were imaged using Zeiss LSM 780-FCS confocal microscope with 405 nm laser.

Immunofluorescence

Migrating T cells were fixed with 3.7% paraformaldehyde (Electron Microscopy Sciences) and blocked and permeabilized for 15 min at room temp (1% BSA and 0.15% Triton X-100 in PBS). Cells were then incubated with fluorescent phalloidin (alexa 568) and DAPI for 45 min at room temp. Cells were then washed three times in block/perm solution, and put in PBS for imaging. 0.5 µm *z*-stacks for a total of 8 µm were collected at 63x from the coverglass moving up through the cell. Each z-slice was background subtracted and the image was projected.

Cell preparation for single-molecule imaging

Cells were cultured in HL5 medium in the presence of 50 µg/mL Doxycycline for 8 h at 21 °C. During the final 1 h, the medium was supplemented with HaloTag® TMR ligand (Promega) at the final concentration of 40 nM. The cells were washed with DB buffer and resuspended in DB buffer at a cell density of 3×10^6 cells/mL. A 10 µL cell suspension was placed on a coverslip (25 mm diameter, 0.12–0.17 mm thick; Matsunami) that was washed by sonication in 0.1 N KOH for 30 min and rinsed with 100% ethanol prior to use. After a 10 min incubation, the cells were overlaid with an agarose sheet (8×8 mm^2, Agarose II; Dojindo). After 20 min of incubation, the coverslip was set in an Attofluor™ cell chamber (Invitrogen) and observed by TIRF Microscope.

Microscopy setup for single-molecule imaging

The methods for single-molecule imaging are described elsewhere[26]. In brief, objective-type TIRFM was constructed on an inverted fluorescence microscope (Ti; Nikon) equipped with two EM-CCD cameras (iXon3; Andor), solid-state CW lasers (OBIS 488-150 LS and OBIS 561-150 LS; Coherent), and an objective lens (CFI Apo TIRF 60X Oil, N.A. 1.49; Nikon). The PIP5K-Halo and RBD-GFP images were acquired at 30 and 1 frames/s, respectively, with a software (iQ2; Andor).

Image analysis

All images were analyzed with Fiji/ImageJ 1.52i (NIH) and/or Python v3.10 (with `numpy`, `scipy`, `pandas`, `scikit-image`, `opencv`, `pillow`, along with standard Python libraries). We utilized Python v3.10 (with Seaborn and/or Matplotlib library), GraphPad Prism 10 (GraphPad), OriginPro v.9.0 (Originlab Corporation), Membrane Kymograph Generator v0.0.1[139], LibreOffice Calc (The Document Foundation), and Microsoft Excel (Microsoft) for plotting our results.

Hierarchical classification of cellular morphologies: First, for each of the N cells, time-lapse image series were obtained from microscope raw data. Second, each of these image series were segmented with a custom-written segmentation pipeline that involved ROI selection (to segregate cells coming in contact with each other), thresholding/binarization, multiple morphological processing steps including dilation, erosion, fill hole, and despeckle. Third, each of these binarized image series were processed with a custom-written montaging pipeline that augmented different image series and provided a specified padding between each of these cells to ultimately result a single large time-series of images for further unbiased processing. In the final of preprocessing, a custom-written Jython script was used to generate and export "labeled" images (where each label corresponds to a particular cell across time-series) using Trackmate Nearest-Neighbor tracker in a headless, automated way. In the hierarchical classification workflow, for each cell across the entire time series, multiple morphological parameters are obtained using `scikit-image measure.regionprops` function and further secondary metrics were computed from there to finally obtain the values of areas, rolling coefficient of variation of areas, circularity, aspect ratio, angle of orientation, angle displacement, angle between the displacement vector and orientation vector (and its rolling coefficient of variation). Based on the kernel density estimation plots of these parameters, specific threshold values were decided for each, as shown in Supplementray Figs. 1 and 2 (please see figure legends there). We used a combination of these parameters to categorize cells into one of the five final categories (based on the modal value for each cell over time): Ameboid, Spiky, Round, Oscillator, and Fan/Keratocyte like. For more details and complete code, please visit the GitHub repo associated with the paper.

Kymographs: For the membrane kymographs, the cells were segmented against the background following standard image-processing steps in Fiji/ImageJ (as described previously in details[26]) or with custom code written in Python v3.10. The kymographs were created from the segmented cells using "Membrane Kymograph Generator" GUI software[139] which implements a custom rotational offset minimization algorithm for aligning boundaries between consecutive frames. Line kymographs that accompanied ventral waves were generated in Fiji/ImageJ by drawing a thick line with a line width of 8–12 pixels and processing the entire stack in the 'KymographBuilder' plugin.

t-stacks: The Fiji/ImageJ was used for for generating the t-stacks. First, time-lapse videos were opened and saved as.avi in Fiji. Next, using the 3D Viewer plugin, frames of the movie were stacked. Importantly, the resampling factor = 1 was used to visualize unblurred activities between frames. If some cytosolic activities were needed to be observed, "Change Transparency" option of 3D viewer plugin was used.

Line-scan intensity profile: For line scans, a straight-line segment was drawn inside the cells with a line width of 6–12 pixels so avoid acquiring any outlier single-pixel values alone. The "Plot Profile" option was used to obtain average intensity values along that thick line across different channels. The values were then saved, normalized, smoothened (using some adjacent-averaging methods with appropriate boundary conditions), renomalized as required, and plotted in OriginPro 9.0 or Python v3.10. For any particular line scan, to maintain consistency, data across different channels were processed in exactly same fashion.

Membrane to cytosol ratio quantification: The cytosol of cells was first outlined with freehand selection tool in Fiji/ImageJ (NIH). The mean intensity of the cytosol was measured using "Measure" function. Then "Make Band" function was applied to the outline the plasma membrane and suitable band size was applied according to the cells.

Then the membrane intensity was measured using the same method and mean values were obtained.

Cell migration analysis: The profiles of migrating cells were analyzed either by segmenting the cells from background in Fiji/ImageJ and using 'Analyzed particles' option (as described in detail elsewhere[25,26,124]), or by using "Manual Tracking" plugin of Fiji/ImageJ, or by custom-written Python based workflow (available in GitHub repo), as appropriate. The color-coded temporal overlay profiles were generated in Fiji/ImageJ by using "Outline" option on binarized cell masks and then processing through 'Temporal-Color Code' option. For all migration tracking plots, the first time point was set to origin. To generate each data points on the velocity boxplots, the Euclidean distances was divided by time interval and then averages were computed for the overall course of the experiment.

Statistical analysis of single-molecule trajectories

The fluorescent images of single molecules were tracked with a laboratory-made software to yield the x- and y- coordinates of each molecule. The methods for estimating lateral diffusion coefficient and membrane-binding lifetime are described elsewhere[26,91]. Briefly, diffusion coefficient was estimated by fitting the statistical distribution of the displacement, Δr, that a single molecule moved during a time interval, $\Delta t = 33.3$ ms, to the following probability density function,

$$P_m(\Delta r) = \sum_{h=1}^{m} q_h \frac{\Delta r}{2D_h\Delta t + 2\varepsilon^2} e^{\left(\frac{-\Delta r^2}{4D_h\Delta t + 4\varepsilon^2}\right)}$$

where D_h, q_h, m, and e denote the diffusion coefficient and fraction of the h-th mobility state, total number of mobility states, and standard deviation of the measurement error, respectively. Short-range diffusion coefficient, D_{SRD}, of an excerpt of a trajectory for 0.5 s was estimated by fitting the mean square displacement (MSD) with the linear function,

$$MSD(t) = 4D_{SRD}t + c$$

where c is a constant representing the measurement error. The membrane-binding lifetime was quantified based on the statistical distribution of the time a single molecule was detected on the membrane. The distribution in cumulative form was fitted to an exponential function as,

$$F(t) = \sum_{j=1}^{n} a_j e^{-(k_j + k_b)t},$$

where k_j, a_j, n, and k_b denote the decaying rate constant of the j-th binding state, the fraction of the j-th binding state, the total number of binding states, and the rate constant of photobleaching of TMR, respectively. The fraction of the molecules that adopt the j-th state at an arbitrary time point was calculated as,

$$f_j = \frac{a_j/k_j}{\sum_{j=1}^{n} a_j/k_j}$$

whereas a mean of the membrane binding lifetime was calculated as,

$$\bar{\tau} = \sum_{j=1}^{n} f_j/k_j$$

Reaction-diffusion model

Core excitable network: The simulations are based on a model whose core consists of three interacting species–Ras, PIP2 (PI(4,5)P2), and PKB (Akt/PKBs)–which together form an excitable network[16]. The concentrations of these species are governed by stochastic reaction-diffusion partial differential equations:

$$\frac{\partial[\mathrm{Ras}]}{\partial t} = -(a_1 + a_2[\mathrm{PKB}])[\mathrm{Ras}] + \frac{a_3}{1 + a_4^2[\mathrm{PIP2}]^2} + a_5 + w_{\mathrm{Ras}} + D_{\mathrm{Ras}}\nabla^2[\mathrm{Ras}] \quad (1a)$$

$$\frac{\partial[\mathrm{PIP2}]}{\partial t} = -(b_1 + b_2[\mathrm{Ras}])[\mathrm{PIP2}] + b_3 + w_{\mathrm{PIP2}} + D_{\mathrm{PIP2}}\nabla^2[\mathrm{PIP2}] \quad (1b)$$

$$\frac{\partial[\mathrm{PKB}]}{\partial t} = -c_1[\mathrm{PKB}] + c_2[\mathrm{Ras}] + w_{\mathrm{PKB}} + D_{\mathrm{PKB}}\nabla^2[\mathrm{PKB}] \quad (1c)$$

Here, D_* denotes the diffusion coefficient of each species, and ∇^2 is the spatial Laplacian, implemented in one spatial dimension along the membrane. The diffusion terms capture spatial redistribution of the molecular species, whereas the stochastic terms w_* represent intrinsic molecular fluctuations. These fluctuations were modeled using a Langevin approximation, with amplitudes determined by the corresponding reaction rates following Gillespie-type formulations[140]. For example, the noise term for PKB was modeled as:

$$w_{\mathrm{PKB}}(t) = \alpha\sqrt{c_1[\mathrm{PKB}] + c_2[\mathrm{Ras}]} \times w(t)$$

where $w(t)$ is Gaussian white-noise process with zero mean and unit variance. The parameter α is an empirical scaling factor used to adjust the magnitude of the noise in simulations.

The terms in the Ras equation represent delayed negative feedback through PKB and mutual antagonism with PIP2. Specifically, Ras activates PKB through Eq. 1c, and PKB in turn inhibits Ras, while Ras suppresses PIP2 and PIP2 inhibits Ras activation. The mutual antagonism between Ras and PIP2 creates an effective positive feedback loop at the level of the reduced system. In the absence of diffusion and stochasticity, and assuming quasi-steady-state behavior for PIP2, we obtain

$$[\mathrm{PIP2}] = \frac{b_3}{b_1 + b_2[\mathrm{Ras}]} \approx \frac{(b_3/b_2)}{[\mathrm{Ras}]}$$

when $b_1 \ll b_2[\mathrm{RAS}]$. Note that b_2 represents Ras-dependent PIP2 depletion, possibly through PI3K. Substituting this expression into the Ras equation yields a nonlinear activation term of the form

$$\frac{a_3[\mathrm{Ras}]^2}{[\mathrm{Ras}]^2 + a_4^2 b_3^2/b_2^2} + a_5$$

so that the reduced system behaves as an excitable two-variable network analogous to FitzHugh–Nagumo-type dynamics.

In this reduced representation, the Ras nullcline becomes cubic-like, while the PKB equation provides the slower recovery variable (Supplementary Fig. 29L–N). We chose parameters such that the two nullclines intersect at a single stable fixed point with low Ras and PKB activity, positioned near the lower turning point of the Ras nullcline. Together with the slow PKB dynamics, this produces excitable behavior. Importantly, changes in parameter values can shift the system into other dynamical regimes, including oscillatory behavior when the fixed point becomes unstable, or a high-activity steady state in which both Ras and PKB remain elevated. In the full ODE model, sufficiently strong feedback can also produce a saddle-node bifurcation and bistability (Supplementary Fig. 29L–N).

PIP5K Dynamics via Ras-Regulated State Transitions: We modeled PIP5K as existing in two interconverting states: a membrane-bound fraction, $\mathrm{PIP5K_{mem}}$, and a cytosolic fraction, $\mathrm{PIP5K_{cyto}}$, with low and high diffusivity, respectively[26,141]. The total amount of PIP5K was conserved within the cell, although its local membrane distribution could vary over space and time. Interconversion between the two states was

regulated by Ras activity, which promoted the transition from $PIP5K_{mem}$ to $PIP5K_{cyto}$. The spatiotemporal dynamics of PIP5K were therefore described by:

$$\frac{\partial[\mathrm{PIP5K_{mem}}]}{\partial t} = -\left(\frac{[\mathrm{Ras}]^2}{d_1+[\mathrm{Ras}]^2}\right)[\mathrm{PIP5K_{mem}}] + d_2[\mathrm{PIP5K_{cyto}}] + D_{\mathrm{PIP5K_{mem}}}\nabla^2[\mathrm{PIP5K_{mem}}] \quad (2a)$$

$$\frac{\partial[\mathrm{PIP5K_{cyto}}]}{\partial t} = -d_2\left[\mathrm{PIP5K_{cyto}}\right] + \left(\frac{[\mathrm{Ras}]^2}{d_1+[\mathrm{Ras}]^2}\right)[\mathrm{PIP5K_{mem}}] + D_{\mathrm{PIP5K_{cyto}}}\nabla^2[\mathrm{PI5K_{cyto}}] \quad (2b)$$

We did not include noise terms in these equations. The sum of the reaction terms in Eqs. 2a and 2b is zero, ensuring conservation of total PIP5K. Because the cytosolic pool is highly diffusible, Ras-dependent removal of PIP5K from one membrane region effectively redistributes it to other regions of the cell.

Functionally, membrane-associated PIP5K enhances PIP2 production by modulating the effective PIP2 production term in Eq. 1b:

$$b_3 \to b_3(1+d_3)\left[\mathrm{PIP5K_{mem}}\right] \quad (2c)$$

This coupling creates the double-negative feedback loop: (Ras ⊣ $PIP5K_{mem}$ → PIP2 ⊣ Ras), thereby strengthening the excitable circuit. Because the Ras-dependent dissociation term is nonlinear, the effect of Ras on PIP5K is strongest in regions of high Ras activity. In addition, since $PIP5K_{mem}$ was assumed not to diffuse rapidly, the inhibitory effect is spatially local. As a result, local Ras activation can reduce PIP5K-mediated PIP2 production at the active site, while the redistributed PIP5K can increase PIP2 production elsewhere, thereby helping establish complementary membrane domains and polarity.

Cytoskeleton feedback loops: To connect the biochemical circuit to downstream cytoskeletal and mechanical responses, we included three additional feedback modules representing branched actin (P_{Actin}) and myosin (P_{Myosin}). Because the actin cytoskeleton is not explicitly modeled, branched actin was represented by a PKB-dependent variable[16]:

$$\frac{\partial[\mathrm{P_{Actin}}]}{\partial t} = -p_1[\mathrm{P_{Actin}}] + p_2[\mathrm{PKB}] + D_{P_{\mathrm{Actin}}}\nabla^2[\mathrm{P_{Actin}}] \quad (3)$$

This term captures local positive feedback from the Ras–PKB pathway to actin assembly. Myosin-based negative feedback was modeled as:

$$\frac{\partial[\mathrm{P_{Myosin}}]}{\partial t} = -p_3[\mathrm{P_{Myosin}}] + p_4[\mathrm{PIP2}] + D_{\mathrm{P_{Myosin}}}\nabla^2[\mathrm{P_{Myosin}}] \quad (4)$$

This term reflects the inhibitory influence of PIP2-associated contractile activity on Ras signaling.

In addition, we modeled an additional inhibitor as a spatially uniform variable driven by the spatially averaged PKB activity:

$$\frac{\partial[P_{GI}]}{\partial t} = -e_1[P_{GI}] + e_2\mathrm{mean}([\mathrm{PKB}]) \quad (5)$$

This term provides a global inhibitory feedback. Together, these feedback modules modulate the Ras equation by increasing or decreasing its effective activation and inhibition terms.

$$(a_1+a_2[\mathrm{PKB}])[\mathrm{Ras}] \mapsto (a_1+a_2[\mathrm{PKB}])[\mathrm{Ras}] \times \left(1+p_m\left[\mathrm{P_{Myosin}}\right]\right) \quad (6)$$

$$\frac{a_3}{1+a_4^2[\mathrm{PIP2}]^2}+a_5 \mapsto \left(\frac{a_3}{1+a_4^2[\mathrm{PIP2}]^2}+a_5\right) \times \left(1+p_a\left(\left[\mathrm{P_{Actin}}\right]-p_{GI}[P_{GI}]\right)\right) \quad (7)$$

In particular, branched actin acts as a local positive feedback loop (Ras → PKB → Actin → Ras), myosin provides local double-negative feedback (Ras ⊣ PIP2 → Myosin ⊣ Ras), and P_{GI} provides a global, negative feedback loop (Ras → PKB → P_{GI} ⊣ Ras). These modules were included to reproduce the observed coupling between signaling dynamics and cell-shape changes, but they are not required for the minimal symmetry-breaking circuit itself.

A final point is that these feedback loops can affect the system on different spatial scales because of diffusion. The branched actin- and myosin-mediated feedbacks are local, because P_{Actin} and P_{Myosin} diffuse relatively slowly and remain confined near the regions where they are generated. Thus, branched actin reinforces front-like signaling locally, myosin stabilizes rear-like signaling locally, and global inhibition prevents system-wide hyperactivation.

Modeling perturbations: Perturbations in Fig. 7 and Supplementary Figs. 28, 29 were simulated by modifying the reaction terms associated with the relevant species or feedback loops during the simulation. Perturbations were implemented by modifying the relevant reaction rates or total pools while keeping the remainder of the model fixed.

PIP5K overexpression: This was modeled by increasing the total cellular PIP5K pool. In the simulations, the total PIP5K concentration was set to 0.1508, corresponding to approximately a 1.9-fold increase relative to wild type.

piki- fan phenotype. The fan-shaped phenotype observed upon PIP5K loss was modeled by reducing the total PIP5K pool to 0.0397 and increasing the strength of actin-mediated Ras activation and decreasing PKB-mediated Ras inhibition. Specifically, p_a was set to 1.25 and p_{GI} to 0.75. Relative to wild type, this corresponds to approximately a 50% reduction in PI(4,5)P2 synthesis activity, a 4.5-fold increase in Ras activation by actin, and a 20% reduction in global, PKB-mediated Ras inhibition. (Note as a simple way to produce a partial reduction of PI(4,5)P2, we reduced PIP5K level to 50% relative to WT.)

piki- oscillator phenotype. The oscillatory phenotype observed under stronger PIP5K depletion was modeled by reducing the total PIP5K pool to 0.0016 and adjusting the feedback strengths to further weaken the stabilizing influences of actin, myosin, and global inhibition. In this regime, p_a was set to 0.1250, p_m to 0.0750, and p_{GI} to 0.75. Relative to wild type, this corresponds to approximately a 98% reduction in PIP5K total, a 2-fold reduction in actin-mediated Ras activation, a 2-fold reduction in myosin-mediated Ras inhibition, and a 20% reduction in global, PKB-mediated Ras inhibition.

Latrunculin treatment. Actin and myosin depletion were simulated by setting $p_1 = 0$ and $p_3 = 0$, thereby blocking the production of actin and myosin downstream of PKB and PIP2, respectively.

Acute PIP5K depletion. Acute elimination of PIP5K was simulated by adding a degradation term to both PIP5K species:

$$\left(\frac{\partial[\mathrm{PIP5K_*}]}{\partial t}\right)_{\mathrm{new}} = \left(\frac{\partial[\mathrm{PIP5K_*}]}{\partial t}\right)_{\mathrm{old}} - 0.2[\mathrm{PIP5K_*}]$$

for both membrane-bound and cytosolic PIP5K.

Acute PIP5K increase. Acute PIP5K elevation was simulated by adding a constant source term to both membrane-bound and cytosolic PIP5K species:

$$\left(\frac{\partial[\mathrm{PIP5K_*}]}{\partial t}\right)_{\mathrm{new}} = \left(\frac{\partial[\mathrm{PIP5K_*}]}{\partial t}\right)_{\mathrm{old}} + 0.001 - 0.2[\mathrm{PIP5K_*}]$$

Myosin and actin perturbations. Elimination of myosin was simulated by setting $p_4 = 0$ and $p_m = 0$. Elimination of actin was simulated by setting $p_2 = 0$ and $p_a = 0$.

Level set-based modeling of cell shape evolution

To evaluate how molecular perturbations affect cell morphology, we simulated cell shape evolution using a level set framework, as previously described[16,94]. In this approach, the cell boundary is represented as the zero-level set of a potential function $\varphi(x,t), x \in \mathbb{R}^2$. The evolution of this potential function over time is governed by:

$$\frac{\partial \varphi(x,t)}{\partial t} + v(x,t).\nabla\varphi(x,t) = 0 \tag{8}$$

where, $v(x,t)$ is the local velocity field derived from mechanical responses to the applied stresses. To compute the velocity field, we used a viscoelastic model that accounts for deformation of both the membrane and the underlying cortex. The displacements of the membrane and cortex, x_{mem} and x_{cort}, were described by:

$$\dot{x}_{\mathrm{mem}} = -\left(\frac{K}{D}\right)x_{\mathrm{cort}} + \left(\frac{1}{D}+\frac{1}{B}\right)\sigma_{\mathrm{tot}} \tag{9a}$$

$$\dot{x}_{\mathrm{cort}} = -\left(\frac{K}{D}\right)x_{\mathrm{cort}} + \left(\frac{1}{D}\right)\sigma_{\mathrm{tot}} \tag{9b}$$

where σ_{tot} is the total stress acting on the cell boundary, and $K, D,$ and B represent the elasticand viscous properties of the membrane and cytoplasm. The boundary velocity used in Eq. (8) is obtained from $\dot{x}_{\mathrm{mem}}$.

The total stress σ_{tot} includes contributions from:

Cortical tension: $\sigma_{\mathrm{ten}} = \gamma\kappa(x)$, where γ is the local cortical tension, and $\kappa(x)$ is the local membrane curvature.

Volume conservation: $\sigma_{\mathrm{vol}} = k_{\mathrm{area}}(A(t) - A_0)$, which penalizes deviations from the initial enclosed area A_0.

Protrusive forces: $\sigma_{\mathrm{pro}} = \sigma_0 R(\theta)$, where $R(\theta)$ is the scaled input from the reaction-diffusion model and σ_0 converts this into an effective protrusive pressure. We defined$R(\theta) = \min(\max(\mathrm{PKB}(\theta) - 0.3, 0), 0.25)$ to constrain protrusive forces to the experimentally observed range of 0.5-5 nN/μm².

Together, these terms allowed us to couple local signaling activity to global cell-shape changes and to simulate the morphological consequences of perturbing the underlying signaling network.

Implementing the simulations: Simulations were performed in MATLAB 2025a (MathWorks, Natick, MA) using custom code based on the Itô formulation implemented via the Stochastic Differential Equation Toolbox (http://sdetoolbox.sourceforge.net). The simulations were used to reproduce membrane fluorescence patterns observed in single-cell confocal images. To reflect the spatial scale of a typical cell, we assumed a cell radius of 5 μm and discretized the membrane into 314 grid points under periodic boundary conditions, corresponding to a spatial resolution of approximately 0.1 μm. Initial conditions were obtained by solving the steady-state equations of the full model, assuming that the dynamics of PIP2, actin, actomyosin, PIP5K, and P_{GI} are sufficiently slow to be approximated as quasi-steady state. The temporal resolution was 1 ms. Total simulation time was 900 s, and kymograph results were generated from a 300 s window after exclusion of initial transients. Level set simulations were performed using the Level Set Toolbox for MATLAB with first-order forward Euler time integration. Parameter values are listed in Supplementary Data 1.

Statistics and reproducibility

Every box plot was generated by a script `halfviolinplot.py` (available in the GitHub repo associated with the paper), which is essentially a wrapper around `seaborn.boxplot` and `seaborn.violinplot` functions of the Seaborn Python library. Hence, box and whisker plots follow standard seaborn/Tukey convention. Box lower edge: $Q1$ = 25th percentile; Box upper edge: Q3 = 75th percentile; Line inside box: median = 50th percentile; Box height: IQR = $Q3$–$Q1$; Lower whisker: the smallest observed data value ≥ $Q1$–1.5 × IQR; Upper whisker: the largest observed data value ≤ $Q3$ + 1.5 × IQR. Points beyond whiskers: individual outliers. All statistical analyses were performed either in Python 3.10 (using SciPy library) or in GraphPad Prism 9. For time-series plots, mean ± s.e.m. or mean ± s.d. were graphed, as indicated in figure legends. For p values, we have consistently used the following conventions: n.s. (not significant), $P > 0.05$; $^{*}P \le 0.05$; $^{**}P \le 0.01$; $^{***}P \le 0.001$; and $^{****}P \le 0.0001$. All microscopy images are representative of $N \ge 3$ independent experiments using biological replicates.

Reporting summary

Further information on research design is available in the Nature Portfolio Reporting Summary linked to this article.

Data availability

All data needed to evaluate the conclusions in the paper are present in the main text or the supplementary materials. Any additional requests for information or data will be fulfilled by the corresponding author upon reasonable request. Source data are provided with this paper.

Code availability

Computational simulation and image analysis codes are available on GitHub: https://github.com/tatsatb/PIP5K-Ras-bistability-symmetry-breaking. The codes are also archived on Zenodo[142] (https://doi.org/10.5281/zenodo.22120967). Any additional information will be available from the corresponding author on reasonable request.

References

1. Luster, A. D., Alon, R. & von Andrian, U. H. Immune cell migration in inflammation: present and future therapeutic targets. *Nat. Immunol.* **6**, 1182–1190 https://doi.org/10.1038/ni1275 (2005).
2. Friedl, P. & Wolf, K. Tumour-cell invasion and migration: diversity and escape mechanisms. *Nat. Rev. Cancer* **3**, 362–374 https://doi.org/10.1038/nrc1075 (2003).
3. Zhan, H. et al. Self-organizing glycolytic waves tune cellular metabolic states and fuel cancer progression. *Nat. Commun.* **16**, 5563 https://doi.org/10.1038/s41467-025-60596-6 (2025).
4. Ridley, A. J. et al. Cell migration: integrating signals from front to back. *Science* **302**, 1704–1709 https://doi.org/10.1126/science.1092053 (2003).
5. Swaney, K. F., Huang, C. H. & Devreotes, P. N. Eukaryotic chemotaxis: a network of signaling pathways controls motility, directional sensing, and polarity. *Annu. Rev. Biophys.* **39**, 265–289 https://doi.org/10.1146/annurev.biophys.093008.131228 (2010).
6. Bagorda, A. & Parent, C. A. Eukaryotic chemotaxis at a glance. *J. Cell Sci.* **121**, 2621–2624 https://doi.org/10.1242/jcs.018077 (2008).
7. SenGupta, S., Parent, C. A. & Bear, J. E. The principles of directed cell migration. *Nat. Rev. Mol. Cell Biol.* **22**, 529–547 https://doi.org/10.1038/s41580-021-00366-6 (2021).
8. Li, D., Tu, H. & Cai, H. Leading the way: molecular drivers of single-cell migration. *Cold Spring Harb. Perspect. Biol.* **17** https://doi.org/10.1101/cshperspect.a041748 (2025).
9. Gerhardt, M. et al. Actin and PIP3 waves in giant cells reveal the inherent length scale of an excited state. *J. Cell Sci.* **127**, 4507–4517 https://doi.org/10.1242/jcs.156000 (2014).

10. Chao, X. et al. Leep2A and Leep2B function as a RasGAP complex to regulate macropinosome formation. *J. Cell Biol.* **223** https://doi.org/10.1083/jcb.202401110 (2024)
11. Tu, H. et al. The PripA-TbcrA complex-centered Rab GAP cascade facilitates macropinosome maturation in *Dictyostelium*. *Nat. Commun.* **13**, 1787 https://doi.org/10.1038/s41467-022-29503-1 (2022).
12. Liu, H. et al. Macrophage migration and phagocytosis are controlled by kindlin-3's link to the cytoskeleton. *J. Immunol.* **204**, 1954–1967 https://doi.org/10.4049/jimmunol.1901134 (2020).
13. Banerjee, T. et al. Signaling and actin waves at a glance. *J. Cell Sci.* **138** https://doi.org/10.1242/jcs.263634 (2025).
14. Arai, Y. et al. Self-organization of the phosphatidylinositol lipids signaling system for random cell migration. *Proc. Natl. Acad. Sci. USA* **107**, 12399–12404 https://doi.org/10.1073/pnas.0908278107 (2010).
15. Matsuoka, S. & Ueda, M. Mutual inhibition between PTEN and PIP3 generates bistability for polarity in motile cells. *Nat. Commun.* **9**, 4481 https://doi.org/10.1038/s41467-018-06856-0 (2018).
16. Miao, Y. et al. Altering the threshold of an excitable signal transduction network changes cell migratory modes. *Nat. Cell Biol.* **19**, 329–340 https://doi.org/10.1038/ncb3495 (2017).
17. Miao, Y. et al. Wave patterns organize cellular protrusions and control cortical dynamics. *Mol. Syst. Biol.* **15**, e8585 https://doi.org/10.15252/msb.20188585 (2019).
18. Servant, G. et al. Polarization of chemoattractant receptor signaling during neutrophil chemotaxis. *Science* **287**, 1037–1040 https://doi.org/10.1126/science.287.5455.1037 (2000).
19. Parent, C. A., Blacklock, B. J., Froehlich, W. M., Murphy, D. B. & Devreotes, P. N. G protein signaling events are activated at the leading edge of chemotactic cells. *Cell* **95**, 81–91 https://doi.org/10.1016/s0092-8674(00)81784-5 (1998).
20. Neumann, N. M. et al. Coordination of receptor tyrosine kinase signaling and interfacial tension dynamics drives radial intercalation and tube elongation. *Dev. Cell* **45**, 67–82 e66 https://doi.org/10.1016/j.devcel.2018.03.011 (2018).
21. Sasaki, A. T., Chun, C., Takeda, K. & Firtel, R. A. Localized Ras signaling at the leading edge regulates PI3K, cell polarity, and directional cell movement. *J. Cell Biol.* **167**, 505–518 https://doi.org/10.1083/jcb.200406177 (2004).
22. Zhang, S., Charest, P. G. & Firtel, R. A. Spatiotemporal regulation of Ras activity provides directional sensing. *Curr. Biol.* **18**, 1587–1593 https://doi.org/10.1016/j.cub.2008.08.069 (2008).
23. Zhao, M. et al. Electrical signals control wound healing through phosphatidylinositol-3-OH kinase-gamma and PTEN. *Nature* **442**, 457–460 https://doi.org/10.1038/nature04925 (2006).
24. Wang, M. J., Artemenko, Y., Cai, W. J., Iglesias, P. A. & Devreotes, P. N. The directional response of chemotactic cells depends on a balance between cytoskeletal architecture and the external gradient. *Cell Rep.* **9**, 1110–1121 https://doi.org/10.1016/j.celrep.2014.09.047 (2014).
25. Banerjee, T. et al. Spatiotemporal dynamics of membrane surface charge regulates cell polarity and migration. *Nat. Cell Biol.* **24**, 1499–1515 https://doi.org/10.1038/s41556-022-00997-7 (2022).
26. Banerjee, T. et al. A dynamic partitioning mechanism polarizes membrane protein distribution. *Nat. Commun.* **14**, 7909 https://doi.org/10.1038/s41467-023-43615-2 (2023).
27. Iwamoto, K., Matsuoka, S. & Ueda, M. Excitable Ras dynamics-based screens reveal RasGEFX is required for macropinocytosis and random cell migration. *Nat. Commun.* **16**, 117 https://doi.org/10.1038/s41467-024-55389-2 (2025).
28. Yang, H. W., Collins, S. R. & Meyer, T. Locally excitable Cdc42 signals steer cells during chemotaxis. *Nat. Cell Biol.* **18**, 191–201 https://doi.org/10.1038/ncb3292 (2016).
29. Devreotes, P. N. et al. Excitable signal transduction networks in directed cell migration. *Annu. Rev. Cell Dev. Biol.* **33**, 103–125 https://doi.org/10.1146/annurev-cellbio-100616-060739 (2017).
30. Devreotes, P. & Janetopoulos, C. Eukaryotic chemotaxis: distinctions between directional sensing and polarization. *J. Biol. Chem.* **278**, 20445–20448 https://doi.org/10.1074/jbc.R300010200 (2003).
31. Iglesias, P. A. & Devreotes, P. N. Navigating through models of chemotaxis. *Curr. Opin. Cell Biol.* **20**, 35–40 https://doi.org/10.1016/j.ceb.2007.11.011 (2008).
32. Xiong, Y., Huang, C. H., Iglesias, P. A. & Devreotes, P. N. Cells navigate with a local-excitation, global-inhibition-biased excitable network. *Proc. Natl. Acad. Sci. USA* **107**, 17079–17086 https://doi.org/10.1073/pnas.1011271107 (2010).
33. Iglesias, P. A. & Devreotes, P. N. Biased excitable networks: how cells direct motion in response to gradients. *Curr. Opin. Cell Biol.* **24**, 245–253 https://doi.org/10.1016/j.ceb.2011.11.009 (2012).
34. Meinhardt, H. Orientation of chemotactic cells and growth cones: models and mechanisms. *J. Cell Sci.* **112**, 2867–2874 https://doi.org/10.1242/jcs.112.17.2867 (1999).
35. Tang, M. et al. Evolutionarily conserved coupling of adaptive and excitable networks mediates eukaryotic chemotaxis. *Nat. Commun.* **5**, 5175 https://doi.org/10.1038/ncomms6175 (2014).
36. Huang, C. H., Tang, M., Shi, C., Iglesias, P. A. & Devreotes, P. N. An excitable signal integrator couples to an idling cytoskeletal oscillator to drive cell migration. *Nat. Cell Biol.* **15**, 1307–1316 https://doi.org/10.1038/ncb2859 (2013).
37. De Belly, H. et al. Cell protrusions and contractions generate long-range membrane tension propagation. *Cell* **186**, 3049–3061 e3015 https://doi.org/10.1016/j.cell.2023.05.014 (2023).
38. Houk, A. R. et al. Membrane tension maintains cell polarity by confining signals to the leading edge during neutrophil migration. *Cell* **148**, 175–188 https://doi.org/10.1016/j.cell.2011.10.050 (2012).
39. Diz-Munoz, A., Fletcher, D. A. & Weiner, O. D. Use the force: membrane tension as an organizer of cell shape and motility. *Trends Cell Biol.* **23**, 47–53 https://doi.org/10.1016/j.tcb.2012.09.006 (2013).
40. Sitarska, E. et al. Sensing their plasma membrane curvature allows migrating cells to circumvent obstacles. *Nat. Commun.* **14**, 5644 https://doi.org/10.1038/s41467-023-41173-1 (2023).
41. Bisaria, A., Hayer, A., Garbett, D., Cohen, D. & Meyer, T. Membrane-proximal F-actin restricts local membrane protrusions and directs cell migration. *Science* **368**, 1205–1210 https://doi.org/10.1126/science.aay7794 (2020).
42. Gong, B., Johnston, J. D., Thiemicke, A., de Marco, A. & Meyer, T. Endoplasmic reticulum-plasma membrane contact gradients direct cell migration. *Nature* **631**, 415–423 https://doi.org/10.1038/s41586-024-07527-5 (2024).
43. Town, J. P. & Weiner, O. D. Local negative feedback of Rac activity at the leading edge underlies a pilot pseudopod-like program for amoeboid cell guidance. *PLoS Biol.* **21**, e3002307 https://doi.org/10.1371/journal.pbio.3002307 (2023).
44. Fort, L. et al. Fam49/CYRI interacts with Rac1 and locally suppresses protrusions. *Nat. Cell Biol.* **20**, 1159–1171 https://doi.org/10.1038/s41556-018-0198-9 (2018).
45. Wu, Z., Su, M., Tong, C., Wu, M. & Liu, J. Membrane shape-mediated wave propagation of cortical protein dynamics. *Nat. Commun.* **9**, 136 https://doi.org/10.1038/s41467-017-02469-1 (2018).
46. Li, D., Sun, F., Yang, Y., Tu, H. & Cai, H. Gradients of PI(4,5)P(2) and PI(3,5)P(2) jointly participate in shaping the back state of *Dictyostelium* cells. *Front. Cell Dev. Biol.* **10**, 835185 https://doi.org/10.3389/fcell.2022.835185 (2022).

47. Zhan, H. et al. An Excitable Ras/PI3K/ERK signaling network controls migration and oncogenic transformation in epithelial cells. *Dev. Cell* **54**, 608–623.e605 https://doi.org/10.1016/j.devcel.2020.08.001 (2020).
48. Lin, Y. et al. Ras-mediated dynamic and biphasic regulation of cell migration. *Proc. Natl. Acad. Sci. USA* **122**, e2503847122 https://doi.org/10.1073/pnas.2503847122 (2025).
49. Kortholt, A. et al. *Dictyostelium chemotaxis*: essential Ras activation and accessory signalling pathways for amplification. *EMBO Rep.* **12**, 1273–1279 https://doi.org/10.1038/embor.2011.210 (2011).
50. Liu, Y. et al. A Galpha-stimulated RapGEF is a receptor-proximal regulator of *Dictyostelium chemotaxis*. *Dev. Cell* **37**, 458–472 https://doi.org/10.1016/j.devcel.2016.05.001 (2016).
51. Veltman, D. M. et al. A plasma membrane template for macropinocytic cups. *Elife* **5** https://doi.org/10.7554/eLife.20085 (2016).
52. Bloomfield, G. et al. Neurofibromin controls macropinocytosis and phagocytosis in Dictyostelium. *Elife* **4** https://doi.org/10.7554/eLife.04940 (2015).
53. Buckley, C. M. et al. Coordinated Ras and Rac activity shapes macropinocytic cups and enables phagocytosis of geometrically diverse bacteria. *Curr. Biol.* **30**, 2912–2926 e2915 https://doi.org/10.1016/j.cub.2020.05.049 (2020).
54. Lange, M., Prassler, J., Ecke, M., Muller-Taubenberger, A. & Gerisch, G. Local Ras activation, PTEN pattern, and global actin flow in the chemotactic responses of oversized cells. *J. Cell Sci.* **129**, 3462–3472 https://doi.org/10.1242/jcs.191148 (2016).
55. Gerisch, G., Ecke, M., Wischnewski, D. & Schroth-Diez, B. Different modes of state transitions determine pattern in the phosphatidylinositide-actin system. *BMC Cell Biol.* **12**, 42 https://doi.org/10.1186/1471-2121-12-42 (2011).
56. Ecke, M., Prassler, J. & Gerisch, G. Fluctuations of formin binding in the generation of membrane patterns. *Biophys. J.* **122**, 3386–3394 https://doi.org/10.1016/j.bpj.2023.07.014 (2023).
57. Yang, Y. et al. Leep1 interacts with PIP3 and the Scar/WAVE complex to regulate cell migration and macropinocytosis. *J Cell Biol* **220** https://doi.org/10.1083/jcb.202010096 (2021).
58. Sasaki, A. T. et al. G protein-independent Ras/PI3K/F-actin circuit regulates basic cell motility. *J. Cell Biol.* **178**, 185–191 https://doi.org/10.1083/jcb.200611138 (2007).
59. Fukushima, S., Matsuoka, S. & Ueda, M. Excitable dynamics of Ras triggers spontaneous symmetry breaking of PIP3 signaling in motile cells. *J. Cell Sci.* **132** https://doi.org/10.1242/jcs.224121 (2019).
60. Lin, Y. et al. Ras suppression potentiates rear actomyosin contractility-driven cell polarization and migration. *Nat Cell Biol* https://doi.org/10.1038/s41556-024-01453-4 (2024).
61. Gerisch, G., Schroth-Diez, B., Muller-Taubenberger, A. & Ecke, M. PIP3 waves and PTEN dynamics in the emergence of cell polarity. *Biophys. J.* **103**, 1170–1178 https://doi.org/10.1016/j.bpj.2012.08.004 (2012).
62. Masters, T. A., Sheetz, M. P. & Gauthier, N. C. F-actin waves, actin cortex disassembly and focal exocytosis driven by actin-phosphoinositide positive feedback. *Cytoskeleton* **73**, 180–196 https://doi.org/10.1002/cm.21287 (2016).
63. Lokuta, M. A. et al. Type Igamma PIP kinase is a novel uropod component that regulates rear retraction during neutrophil chemotaxis. *Mol. Biol. Cell* **18**, 5069–5080 https://doi.org/10.1091/mbc.e07-05-0428 (2007).
64. Lacalle, R. A. et al. Type I phosphatidylinositol 4-phosphate 5-kinase controls neutrophil polarity and directional movement. *J. Cell Biol.* **179**, 1539–1553 https://doi.org/10.1083/jcb.200705044 (2007).
65. Wills, R. C. & Hammond, G. R. V. PI(4,5)P2: signaling the plasma membrane. *Biochem J.* **479**, 2311–2325 https://doi.org/10.1042/BCJ20220445 (2022).
66. Katan, M. & Cockcroft, S. Phosphatidylinositol(4,5)bisphosphate: diverse functions at the plasma membrane. *Essays Biochem.* **64**, 513–531 https://doi.org/10.1042/EBC20200041 (2020).
67. Kwiatkowska, K. One lipid, multiple functions: how various pools of PI(4,5)P(2) are created in the plasma membrane. *Cell Mol. Life Sci.* **67**, 3927–3946 https://doi.org/10.1007/s00018-010-0432-5 (2010).
68. Hammond, G. R. V. & Burke, J. E. Novel roles of phosphoinositides in signaling, lipid transport, and disease. *Curr. Opin. Cell Biol.* **63**, 57–67 https://doi.org/10.1016/j.ceb.2019.12.007 (2020).
69. Fets, L., Nichols, J. M. & Kay, R. R. A PIP5 kinase essential for efficient chemotactic signaling. *Curr. Biol.* **24**, 415–421 https://doi.org/10.1016/j.cub.2013.12.052 (2014).
70. Wessels, D., Lusche, D. F., Kuhl, S., Heid, P. & Soll, D. R. PTEN plays a role in the suppression of lateral pseudopod formation during Dictyostelium motility and chemotaxis. *J. Cell Sci.* **120**, 2517–2531 https://doi.org/10.1242/jcs.010876 (2007).
71. Iijima, M. & Devreotes, P. Tumor suppressor PTEN mediates sensing of chemoattractant gradients. *Cell* **109**, 599–610 https://doi.org/10.1016/s0092-8674(02)00745-6 (2002).
72. Keizer-Gunnink, I., Kortholt, A. & Van Haastert, P. J. Chemoattractants and chemorepellents act by inducing opposite polarity in phospholipase C and PI3-kinase signaling. *J. Cell Biol.* **177**, 579–585 https://doi.org/10.1083/jcb.200611046 (2007).
73. Loovers, H. M. et al. A diverse family of inositol 5-phosphatases playing a role in growth and development in *Dictyostelium discoideum*. *J. Biol. Chem.* **278**, 5652–5658 https://doi.org/10.1074/jbc.M208396200 (2003).
74. Clark, J. et al. *Dictyostelium* uses ether-linked inositol phospholipids for intracellular signalling. *EMBO J.* **33**, 2188–2200 https://doi.org/10.15252/embj.201488677 (2014).
75. Li, X. et al. Mutually inhibitory Ras-PI(3,4)P(2) feedback loops mediate cell migration. *Proc. Natl. Acad. Sci. USA* **115**, E9125–E9134 https://doi.org/10.1073/pnas.1809039115 (2018).
76. Swaney, K. F., Borleis, J., Iglesias, P. A. & Devreotes, P. N. Novel protein Callipygian defines the back of migrating cells. *Proc. Natl. Acad. Sci. USA* **112**, E3845–E3854 https://doi.org/10.1073/pnas.1509098112 (2015).
77. Kunz, J. et al. The activation loop of phosphatidylinositol phosphate kinases determines signaling specificity. *Mol. Cell* **5**, 1–11 https://doi.org/10.1016/s1097-2765(00)80398-6 (2000).
78. King, J. S. & Kay, R. R. The origins and evolution of macropinocytosis. *Philos. Trans. R. Soc. Lond. B Biol. Sci.* **374**, 20180158 https://doi.org/10.1098/rstb.2018.0158 (2019).
79. Kay, R. R., Lutton, J. E., King, J. S. & Bretschneider, T. Making cups and rings: the 'stalled-wave' model for macropinocytosis. *Biochem. Soc. Trans.* **52**, 1785–1794 https://doi.org/10.1042/BST20231426 (2024).
80. Lutton, J. E. et al. Formation and closure of macropinocytic cups in *Dictyostelium*. *Curr. Biol.* **33**, 3083–3096 e3086 https://doi.org/10.1016/j.cub.2023.06.017 (2023).
81. Kuhn, J. et al. Complementary cytoskeletal feedback loops control signal transduction excitability and cell polarity. *Nat. Commun.* **16**, 7482 https://doi.org/10.1038/s41467-025-62799-3 (2025).
82. Weiner, O. D., Marganski, W. A., Wu, L. F., Altschuler, S. J. & Kirschner, M. W. An actin-based wave generator organizes cell motility. *PLoS Biol.* **5**, e221 https://doi.org/10.1371/journal.pbio.0050221 (2007).
83. Xu, J. et al. Divergent signals and cytoskeletal assemblies regulate self-organizing polarity in neutrophils. *Cell* **114**, 201–214 https://doi.org/10.1016/s0092-8674(03)00555-5 (2003).
84. O'Neill, P. R. & Gautam, N. Subcellular optogenetic inhibition of G proteins generates signaling gradients and cell migration. *Mol.*

Biol. Cell **25**, 2305–2314 https://doi.org/10.1091/mbc.E14-04-0870 (2014).
85. Wu, L., Valkema, R., Van Haastert, P. J. & Devreotes, P. N. The G protein beta subunit is essential for multiple responses to chemoattractants in *Dictyostelium*. *J. Cell Biol.* **129**, 1667–1675 https://doi.org/10.1083/jcb.129.6.1667 (1995).
86. Lilly, P. J. & Devreotes, P. N. Chemoattractant and GTP gamma S-mediated stimulation of adenylyl cyclase in *Dictyostelium* requires translocation of CRAC to membranes. *J. Cell Biol.* **129**, 1659–1665 https://doi.org/10.1083/jcb.129.6.1659 (1995).
87. Weckerly, C. C. et al. PILS-Nir1 is a sensitive phosphatidic acid biosensor that reveals mechanisms of lipid production. *J. Cell Biol.* **224** https://doi.org/10.1083/jcb.202405174 (2025).
88. Wiege, K. et al. Defective macrophage migration in Galphai2- but not Galphai3-deficient mice. *J. Immunol.* **189**, 980–987 https://doi.org/10.4049/jimmunol.1200891 (2012).
89. Peng, G. E., Wilson, S. R. & Weiner, O. D. A pharmacological cocktail for arresting actin dynamics in living cells. *Mol. Biol. Cell* **22**, 3986–3994 https://doi.org/10.1091/mbc.E11-04-0379 (2011).
90. van Haastert, P. J., Keizer-Gunnink, I. & Kortholt, A. Coupled excitable Ras and F-actin activation mediates spontaneous pseudopod formation and directed cell movement. *Mol. Biol. Cell* **28**, 922–934 https://doi.org/10.1091/mbc.E16-10-0733 (2017).
91. Matsuoka, S., Miyanaga, Y. & Ueda, M. Multi-state transition kinetics of intracellular signaling molecules by single-molecule imaging analysis. *Methods Mol. Biol.* **1407**, 361–379 https://doi.org/10.1007/978-1-4939-3480-5_25 (2016).
92. Wolgemuth, C. W. & Zajac, M. The moving boundary node method: a level set-based, finite volume algorithm with applications to cell motility. *J. Comput. Phys.* **229**, 7287–7308 https://doi.org/10.1016/j.jcp.2010.06.014 (2010).
93. Yang, L. et al. Modeling cellular deformations using the level set formalism. *BMC Syst. Biol.* **2**, 68 https://doi.org/10.1186/1752-0509-2-68 (2008).
94. Shi, C., Huang, C. H., Devreotes, P. N. & Iglesias, P. A. Interaction of motility, directional sensing, and polarity modules recreates the behaviors of chemotaxing cells. *PLoS Comput. Biol.* **9**, e1003122 https://doi.org/10.1371/journal.pcbi.1003122 (2013).
95. Kabacoff, C. et al. Dynacortin facilitates polarization of chemotaxing cells. *BMC Biol.* **5**, 53 https://doi.org/10.1186/1741-7007-5-53 (2007).
96. Itoh, T. & Tsujita, K. Exploring membrane mechanics: the role of membrane-cortex attachment in cell dynamics. *Curr. Opin. Cell Biol.* **81** 102173 https://doi.org/10.1016/j.ceb.2023.102173 (2023).
97. Chau, A. H., Walter, J. M., Gerardin, J., Tang, C. & Lim, W. A. Designing synthetic regulatory networks capable of self-organizing cell polarization. *Cell* **151**, 320–332 https://doi.org/10.1016/j.cell.2012.08.040 (2012).
98. Lim, W. A., Lee, C. M. & Tang, C. Design principles of regulatory networks: searching for the molecular algorithms of the cell. *Mol. Cell* **49**, 202–212 https://doi.org/10.1016/j.molcel.2012.12.020 (2013).
99. Lomakin, A. J. et al. Competition for actin between two distinct F-actin networks defines a bistable switch for cell polarization. *Nat. Cell Biol.* **17**, 1435–1445 https://doi.org/10.1038/ncb3246 (2015).
100. Byrne, K. M. et al. Bistability in the Rac1, PAK, and RhoA signaling network drives actin cytoskeleton dynamics and cell motility switches. *Cell Syst.* **2**, 38–48 https://doi.org/10.1016/j.cels.2016.01.003 (2016).
101. De Belly, H. et al. Long-range mutual activation establishes Rho and Rac polarity during cell migration. *Nat. Cell Biol.* **28**, 1244–1257 https://doi.org/10.1038/s41556-026-01965-1 (2026).
102. Kamimura, Y. et al. PIP3-independent activation of TorC2 and PKB at the cell's leading edge mediates chemotaxis. *Curr. Biol.* **18**, 1034–1043 https://doi.org/10.1016/j.cub.2008.06.068 (2008).
103. Hoeller, O. & Kay, R. R. Chemotaxis in the absence of PIP3 gradients. *Curr. Biol.* **17**, 813–817 https://doi.org/10.1016/j.cub.2007.04.004 (2007).
104. Yamaguchi, H. et al. Phosphatidylinositol 4,5-bisphosphate and PIP5-kinase Ialpha are required for invadopodia formation in human breast cancer cells. *Cancer Sci.* **101**, 1632–1638 https://doi.org/10.1111/j.1349-7006.2010.01574.x (2010).
105. Sharma, V. P., DesMarais, V., Sumners, C., Shaw, G. & Narang, A. Immunostaining evidence for PI(4,5)P2 localization at the leading edge of chemoattractant-stimulated HL-60 cells. *J. Leukoc. Biol.* **84**, 440–447 https://doi.org/10.1189/jlb.0907636 (2008).
106. Janmey, P. A. & Stossel, T. P. Modulation of gelsolin function by phosphatidylinositol 4,5-bisphosphate. *Nature* **325**, 362–364 https://doi.org/10.1038/325362a0 (1987).
107. Fukami, K., Endo, T., Imamura, M. & Takenawa, T. alpha-Actinin and vinculin are PIP2-binding proteins involved in signaling by tyrosine kinase. *J. Biol. Chem.* **269**, 1518–1522 (1994).
108. Gilmore, A. P. & Burridge, K. Regulation of vinculin binding to talin and actin by phosphatidyl-inositol-4-5-bisphosphate. *Nature* **381**, 531–535 https://doi.org/10.1038/381531a0 (1996).
109. Rozelle, A. L. et al. Phosphatidylinositol 4,5-bisphosphate induces actin-based movement of raft-enriched vesicles through WASP-Arp2/3. *Curr. Biol.* **10**, 311–320 https://doi.org/10.1016/s0960-9822(00)00384-5 (2000).
110. Di Paolo, G. et al. Recruitment and regulation of phosphatidylinositol phosphate kinase type 1 gamma by the FERM domain of talin. *Nature* **420**, 85–89 https://doi.org/10.1038/nature01147 (2002).
111. Ling, K., Doughman, R. L., Firestone, A. J., Bunce, M. W. & Anderson, R. A. Type Iγ phosphatidylinositol phosphate kinase targets and regulates focal adhesions. *Nature* **420**, 89–93 https://doi.org/10.1038/nature01082 (2002).
112. Papayannopoulos, V. et al. A polybasic motif allows N-WASP to act as a sensor of PIP(2) density. *Mol. Cell* **17**, 181–191 https://doi.org/10.1016/j.molcel.2004.11.054 (2005).
113. El Sayegh, T. Y. et al. Phosphatidylinositol-4,5 bisphosphate produced by PIP5KIgamma regulates gelsolin, actin assembly, and adhesion strength of N-cadherin junctions. *Mol. Biol. Cell* **18**, 3026–3038 https://doi.org/10.1091/mbc.e06-12-1159 (2007).
114. van Rheenen, J. et al. EGF-induced PIP2 hydrolysis releases and activates cofilin locally in carcinoma cells. *J. Cell Biol.* **179**, 1247–1259 https://doi.org/10.1083/jcb.200706206 (2007).
115. Bae, Y. H. et al. Profilin1 regulates PI(3,4)P2 and lamellipodin accumulation at the leading edge thus influencing motility of MDA-MB-231 cells. *Proc. Natl. Acad. Sci. USA* **107**, 21547–21552 https://doi.org/10.1073/pnas.1002309107 (2010).
116. Zhao, H., Hakala, M. & Lappalainen, P. ADF/cofilin binds phosphoinositides in a multivalent manner to act as a PIP(2)-density sensor. *Biophys. J.* **98**, 2327–2336 https://doi.org/10.1016/j.bpj.2010.01.046 (2010).
117. Goni, G. M. et al. Phosphatidylinositol 4,5-bisphosphate triggers activation of focal adhesion kinase by inducing clustering and conformational changes. *Proc. Natl. Acad. Sci. USA* **111**, E3177–E3186 https://doi.org/10.1073/pnas.1317022111 (2014).
118. Kunkl, M. et al. ISA-2011B, a phosphatidylinositol 4-Phosphate 5-Kinase alpha Inhibitor, Impairs CD28-Dependent Costimulatory and Pro-inflammatory Signals in Human T Lymphocytes. *Front. Immunol.* **8**, 502 https://doi.org/10.3389/fimmu.2017.00502 (2017).
119. Sengelaub, C. A., Navrazhina, K., Ross, J. B., Halberg, N. & Tavazoie, S. F. PTPRN2 and PLCbeta1 promote metastatic breast cancer cell migration through PI(4,5)P2-dependent actin remodeling. *EMBO J.* **35**, 62–76 https://doi.org/10.15252/embj.201591973 (2016).

120. Jin, Y. & Xue, J. Lipid kinases PIP5Ks and PIP4Ks: potential drug targets for breast cancer. *Front. Oncol.* **13**, 1323897 https://doi.org/10.3389/fonc.2023.1323897 (2023).
121. Peng, J. M., Lin, S. H., Yu, M. C. & Hsieh, S. Y. CLIC1 recruits PIP5K1A/C to induce cell-matrix adhesions for tumor metastasis. *J. Clin. Investig.* **131** https://doi.org/10.1172/JCI133525 (2021)
122. Semenas, J. et al. The role of PI3K/AKT-related PIP5K1alpha and the discovery of its selective inhibitor for treatment of advanced prostate cancer. *Proc. Natl. Acad. Sci. USA* **111**, E3689–E3698 https://doi.org/10.1073/pnas.1405801111 (2014).
123. Wang, T. et al. PIP5K1alpha is required for promoting tumor progression in castration-resistant prostate cancer. *Front. Cell Dev. Biol.* **10**, 798590 https://doi.org/10.3389/fcell.2022.798590 (2022).
124. Pal, D. S. et al. Actuation of single downstream nodes in growth factor network steers immune cell migration. *Dev. Cell* **58**, 1170–1188 e1177 https://doi.org/10.1016/j.devcel.2023.04.019 (2023).
125. Kreppel, L. et al. dictyBase: a new *Dictyostelium discoideum* genome database. *Nucleic Acids Res.* **32**, D332–D333 https://doi.org/10.1093/nar/gkh138 (2004).
126. Fey, P., Dodson, R. J., Basu, S. & Chisholm, R. L. One stop shop for everything *Dictyostelium*: dictyBase and the Dicty Stock Center in 2012. *Methods Mol. Biol.* **983**, 59–92 https://doi.org/10.1007/978-1-62703-302-2_4 (2013).
127. Lampert, T. J. et al. Shear force-based genetic screen reveals negative regulators of cell adhesion and protrusive activity. *Proc. Natl. Acad. Sci. USA* **114**, E7727–E7736 https://doi.org/10.1073/pnas.1616600114 (2017).
128. Millius, A. & Weiner, O. D. Manipulation of neutrophil-like HL-60 cells for the study of directed cell migration. *Methods Mol. Biol.* **591**, 147–158 https://doi.org/10.1007/978-1-60761-404-3_9 (2010).
129. Rovera, G., Santoli, D. & Damsky, C. Human promyelocytic leukemia cells in culture differentiate into macrophage-like cells when treated with a phorbol diester. *Proc. Natl. Acad. Sci. USA* **76**, 2779–2783 https://doi.org/10.1073/pnas.76.6.2779 (1979).
130. Meshik, X., O'Neill, P. R. & Gautam, N. Optogenetic control of cell migration. *Methods Mol. Biol.* **1749**, 313–324 https://doi.org/10.1007/978-1-4939-7701-7_22 (2018).
131. Bell, G. R. R., Rincon, E., Akdogan, E. & Collins, S. R. Optogenetic control of receptors reveals distinct roles for actin- and Cdc42-dependent negative signals in chemotactic signal processing. *Nat. Commun.* **12**, 6148 https://doi.org/10.1038/s41467-021-26371-z (2021).
132. Sekine, R., Kawata, T. & Muramoto, T. CRISPR/Cas9 mediated targeting of multiple genes in *Dictyostelium*. *Sci. Rep.* **8**, 8471 https://doi.org/10.1038/s41598-018-26756-z (2018).
133. Pal, D. S. et al. Optogenetic modulation of guanine nucleotide exchange factors of Ras superfamily proteins directly controls cell shape and movement. *Front. Cell Dev. Biol.* **11** https://doi.org/10.3389/fcell.2023.1195806 (2023).
134. Suh, B. C., Inoue, T., Meyer, T. & Hille, B. Rapid chemically induced changes of PtdIns(4,5)P2 gate KCNQ ion channels. *Science* **314**, 1454–1457 https://doi.org/10.1126/science.1131163 (2006).
135. Kamimura, Y., Tang, M. & Devreotes, P. Assays for chemotaxis and chemoattractant-stimulated TorC2 activation and PKB substrate phosphorylation in *Dictyostelium*. *Methods Mol. Biol.* **571**, 255–270 https://doi.org/10.1007/978-1-60761-198-1_17 (2009).
136. Cai, H. et al. Nucleocytoplasmic shuttling of a GATA transcription factor functions as a development timer. *Science* **343**, 1249531 https://doi.org/10.1126/science.1249531 (2014).
137. Artemenko, Y., Swaney, K. F. & Devreotes, P. N. Assessment of development and chemotaxis in *Dictyostelium discoideum* mutants. *Methods Mol. Biol.* **769**, 287–309 https://doi.org/10.1007/978-1-61779-207-6_20 (2011).
138. Aufderheide, K. J. & Janetopoulos, C. Migration of *Dictyostelium discoideum* to the chemoattractant folic acid. *Methods Mol. Biol.* **1407**, 25–39 https://doi.org/10.1007/978-1-4939-3480-5_3 (2016).
139. Banerjee, T., Abubaker-Sharif, B., Devreotes, P. N. & Iglesias, P. A. Membrane Kymograph Generator: a cross-platform GUI software for automated generation and analysis of kymographs along dynamic cell boundaries. *Bioinformatics* **42** https://doi.org/10.1093/bioinformatics/btag400 (2026).
140. Gillespie, D. T. The chemical Langevin equation. *J. Chem. Phys.* **113**, 297–306 https://doi.org/10.1063/1.481811 (2000).
141. Banerjee, P. et al. Spatial distribution of cytoskeleton-mediated feedback controls cell polarization: a computational study. *PLoS Comput. Biol.* **21**, e1013036 https://doi.org/10.1371/journal.pcbi.1013036 (2025).
142. tatsatb/PIP5K-Ras-bistability-symmetry-breaking: v0.0.1 v. v0.0.1 (Zenodo, 2026).

Acknowledgements

We thank all members of the Devreotes, Iglesias, and Robinson laboratories (Schools of Medicine and Engineering, JHU) for helpful discussions and for providing resources. We thank Jonathan Kuhn and Yiyan Lin (Devreotes Lab) as well as Elena Parajon (Robinson Lab) for providing constructs. We thank Wakiko Iwata (Iijima Lab, School of Medicine, JHU) for sharing experimental reagents and advice for performing spheroid assay. We thank Orion D. Weiner (UCSF) for providing the HL-60 cell line. We thank Sean Collins (UC Davis) for providing transposon plasmids. We thank Gerald Hammond (U Pittsburgh) for providing the cytosolic PIP5K1C construct. We thank Stephen Gould (School of Medicine, JHU) for help with instrumentation. We appreciate services of DictyBase and Addgene for providing plasmids.

Author contributions

Y.D., T.B., and P.N.D. conceived and designed the project. Y.D. engineered constructs/stable cell lines. Y.D. and T.B. designed and executed the majority of the experiments. T.B. and Y.D. performed quantification and the majority of the data analysis. S.M. and M.U. conducted single-molecule imaging assays, performed the relevant analysis, and helped with RasGEF screening. L.A.K. and N.H.R. conducted primary T cell migration experiments and relevant quantifications. D.S.P. and H.Z. provided resources for mammalian experiments. J.B. and Y.L. made a few constructs and helped with cell culture. D.B. and P.A.I. developed computational models, and D.B. performed simulations with inputs from P.A.I., P.B., P.N.D., T.B., and Y.D. Y.D. and T.B. contributed equally and share the first authorship. S.M. and D.B. contributed equally. T.B., Y.D., and P.N.D. wrote and revised the manuscript with comments from the rest of the authors. P.N.D. supervised the overall study.

Funding

This work was supported by NIH grants R35 GM118177 (to P.N.D.), R01 GM149073 (to P.A.I.), R01 AI185016 (to N.H.R.), S10OD016374 (to S. Kuo of the JHU Microscope Facility), NIH fellowship F31HL182305 (to Y.D.), AFOSR MURI FA95501610052 (to P.N.D.), as well as Japan Science and Technology Agency grant no. JPMJCR21E1 and JPMJKP25V4 (to M.U.). This manuscript is the result of funding in whole or in part by the National Institutes of Health (NIH). It is subject to the NIH Public Access Policy. Through acceptance of this federal funding, NIH has been given a right to make this manuscript publicly available in PubMed Central upon the Official Date of Publication, as defined by NIH.

Competing interests

The authors declare no competing interests.

Additional information

Supplementary information The online version contains supplementary material available at https://doi.org/10.1038/s41467-026-77894-2.

Correspondence and requests for materials should be addressed to Peter N. Devreotes.

Peer review information *Nature Communications* thanks Cornelis Weijer and the other anonymous reviewers for their contribution to the peer review of this work. A peer review file is available.

Reprints and permissions information is available at http://www.nature.com/reprints

Publisher's note Springer Nature remains neutral with regard to jurisdictional claims in published maps and institutional affiliations.

Open Access This article is licensed under a Creative Commons Attribution-NonCommercial-NoDerivatives 4.0 International License, which permits any non-commercial use, sharing, distribution and reproduction in any medium or format, as long as you give appropriate credit to the original author(s) and the source, provide a link to the Creative Commons licence, and indicate if you modified the licensed material. You do not have permission under this licence to share adapted material derived from this article or parts of it. The images or other third party material in this article are included in the article's Creative Commons licence, unless indicated otherwise in a credit line to the material. If material is not included in the article's Creative Commons licence and your intended use is not permitted by statutory regulation or exceeds the permitted use, you will need to obtain permission directly from the copyright holder. To view a copy of this licence, visit http://creativecommons.org/licenses/by-nc-nd/4.0/.

© The Author(s) 2026

[1]Department of Cell Biology and Center for Cell Dynamics, School of Medicine, Johns Hopkins University, Baltimore, MD, USA. [2]Department of Chemical and Biomolecular Engineering, Whiting School of Engineering, Johns Hopkins University, Baltimore, MD, USA. [3]Laboratory of Single Molecule Biology, Graduate School of Science and Graduate School of Frontier Biosciences, Osaka University, Suita, Japan. [4]Laboratory for Computational Sensing and Robotics, Johns Hopkins University, Baltimore, MD, USA. [5]Department of Microbiology and Immunology, State University of New York Upstate Medical University, Syracuse, NY, USA. [6]Department of Physics and Astronomy, Johns Hopkins University, Baltimore, MD, USA. [7] Biological and Biochemistry Programs, The Graduate Center, The City University of New York, New York, NY, USA. [8]Department of Electrical and Computer Engineering, Whiting School of Engineering, Johns Hopkins University, Baltimore, MD, USA. [9]Department of Applied Mathematics and Statistics, Whiting School of Engineering, Johns Hopkins University, Baltimore, MD, USA. [10]Department of Biological Chemistry, School of Medicine, Johns Hopkins University, Baltimore, MD, USA. [11]Present address: Howard Hughes Medical Institute, Whitehead Institute for Biomedical Research, Massachusetts Institute of Technology, Cambridge, MA, USA. [12]Present address: Department of Biological Sciences, Hunter College, The City University of New York, New York, NY, USA. [13]These authors contributed equally: Yu Deng, Tatsat Banerjee. ✉e-mail: pnd@jhmi.edu